The Journal of Chemical Physics

Cite as: J. Chem. Phys. 157, 174204 (2022); https://doi.org/10.1063/5.0105388

Submitted: 23 June 2022 • Accepted: 05 September 2022 • Accepted Manuscript Online: 13

September 2022 • Published Online: 07 November 2022

🗓 Alec A. Beaton, 🗓 Alexandria Guinness and 🗓 John M. Franck

COLLECTIONS

EP This paper was selected as an Editor's Pick







ARTICLES YOU MAY BE INTERESTED IN

Quantum mechanics of open systems: Dissipaton theories

The Journal of Chemical Physics 157, 170901 (2022); https://doi.org/10.1063/5.0123999

Many recent density functionals are numerically ill-behaved

The Journal of Chemical Physics 157, 174114 (2022); https://doi.org/10.1063/5.0121187

Atomistic structure search using local surrogate model

The Journal of Chemical Physics 157, 174115 (2022); https://doi.org/10.1063/5.0121748

The Journal of Chemical Physics Special Topics Open for Submissions



A modernized view of coherence pathways applied to magnetic resonance experiments in unstable, inhomogeneous fields 💷

Cite as: J. Chem. Phys. 157, 174204 (2022); doi: 10.1063/5.0105388 Submitted: 23 June 2022 • Accepted: 5 September 2022 • **Published Online: 7 November 2022**









Alec A. Beaton, D Alexandria Guinness, D and John M. Franck D





AFFILIATIONS

Department of Chemistry, Syracuse University, Syracuse, New York 13210, USA

a) Author to whom correspondence should be addressed: jmfranck@syr.edu

ABSTRACT

This article presents a standardized alternative to the traditional phase cycling approach employed by the overwhelming majority of contemporary Nuclear Magnetic Resonance (NMR) research. On well-tested, stable NMR systems running well-tested pulse sequences in highly optimized, homogeneous magnetic fields, the hardware and/or software responsible for traditional phase cycling quickly isolate a meaningful subset of data by averaging and discarding between 3/4 and 127/128 of the digitized data. In contrast, the new domain colored coherence transfer (DCCT) approach enables the use of all the information acquired from all transients. This approach proves to be particularly useful where multiple coherence pathways are required, or for improving the signal when the magnetic fields are inhomogeneous and unstable. For example, the authors' interest in the nanoscale heterogeneities of hydration dynamics demands increasingly sophisticated and automated measurements deploying Overhauser Dynamic Nuclear Polarization (ODNP) in low-field electromagnets, where phase cycling and signal averaging perform suboptimally. This article demonstrates the capabilities of DCCT on ODNP data and with a collection of algorithms that provide robust phasing, avoidance of baseline distortion, and the ability to realize relatively weak signals amid background noise through signal-averaged correlation alignment. The DCCT schema works by combining a multidimensional organization of phase cycled data with a specific methodology for visualizing the resulting complex-valued data. It could be extended to other forms of coherent spectroscopy seeking to analyze multiple coherence transfer pathways.

Published under an exclusive license by AIP Publishing. https://doi.org/10.1063/5.0105388

I. INTRODUCTION

This article focuses on a comprehensive, nonstandard approach to processing and presenting data from the various coherence pathways accessed by a Magnetic Resonance (MR) experiment. This formalized approach—i.e., "schema"—significantly improves the speed with which spectroscopists can develop new types of experiments. It offers particular advantages when confronted with unpredictably time-varying magnetic fields or samples with very low proton content. Furthermore, it can guide the development of routines that improve data quality. This article presents examples from the authors' lab, where the schema was integral to developing routine, quality Overhauser Dynamic Nuclear Polarization (ODNP) acquisition, with particular focus on mitigating the effects of inhomogeneity and time instability of the fields offered by conventional room temperature electromagnets.

ODNP represents an example of a powerful technique that could benefit from the techniques introduced here. Despite the rapid, sub-nanosecond exchange of hydration water with bulk water, ODNP has the capability to measure the variation in the dynamics of hydration water molecules at specific sites, selected with nanometer-scale specificity, 1,2 as well as the accessibility of those sites to water.^{3,4} The spectroscopist can choose sites based on the location of a small molecule within a heterogeneous mixture by linking labels to the surface of a macromolecule or by linking them within the core of a macromolecule (or macromolecular assembly).^{5,6} Previous literature has advocated ODNP as a tool for analyzing the hydration layer for more than 12 years.^{7,8} Furthermore, the technique employs relatively low magnetic fields (typically 0.35 T), permitting dissemination in concert with cw Electron Spin Resonance (ESR) spectroscopy^{1,2} and extension to permanent magnet systems, ^{7,9,10} making it an eminently customizable technique. Nonetheless, ODNP has not vet been widely adopted for studying the hydration layer. We ascribe this discrepancy in part to the practical barriers imposed by the differences between ODNP and more traditional Nuclear Magnetic Resonance (NMR) methods: the need to conduct ODNP at lower field, where sources of magnetic fields tend to be inhomogeneous and unstable, and where phase cycling and signal averaging may prove suboptimal. Furthermore, a full analysis of the dynamics available from ODNP involves collection of both a series of measurements of spin polarization at different levels of microwave (ESR) saturation (progressive enhancement) and several inversion recovery experiments, resulting in a relatively large quantity of data under consideration. As a consequence, we developed the data processing schema presented here, which—while certainly useful for ODNP work-can be extended to a number of magnetic resonance experiments and which we, therefore, present in a generalized manner.

ODNP must be performed at low fields in order to obtain information on the solvent dynamics. Low fields ensure that ODNP cross-relaxation exclusively samples the translational dynamics of the solvent.¹¹ In contrast, at higher fields, ^{12,13} cross-relaxation due to translational motion falls to negligible levels and the effects of intramolecular motions of the spin label¹⁴ or even correlated motions¹⁵ then control the remaining cross-relaxation. Most hardware configurations that supply low fields rely on electromagnets or permanent magnets, both of which produce fields that tend to be inhomogeneous and unstable, giving rise to a host of practical challenges. For particular sample configurations, one can achieve reasonable ODNP results with mostly commercial hardware.^{2,11} Recent studies have demonstrated spectral resolution without the need for added shim coils, 10 while others have implemented a practicable shim stack.¹⁹ Importantly, thus far, all such advances detail engineering of the spectrometer device itself rather than offering strategies for finer control of data visualization and processing, which could apply to all instruments. This article addresses the latter

Overall, the development of emerging MR techniques such as ODNP spectroscopy mandates a new approach to conventional NMR. Thus, this article carefully draws fundamental concepts of coherence transfer (CT) from the original literature, ^{20–25} vation from more recent efforts, 26-28 to formalize an improvement upon traditional phase cycling in MR, in which standard code can quickly acquire, organize, and present signals in a wide range of contexts while maximizing the information presented. The concept of phase cycling goes back decades.^{20–25} However, conventional phase cycling seeks to select the desired CT pathway of interest as quickly and efficiently as possible while discarding all other information. As previously noted, ^{26–28} this choice was originally motivated by now-antiquated hardware. Contributions toward utilizing the theory of quantum CT²⁹ and phase cycling²⁵ have been revisited in the past two decades on various occasions, ^{26–28,30,31} and the recommendation of forgoing cycling of the receiver phase and separately storing each acquired transient has repeatedly arisen. Such methods rely on post-acquisition processing to select the CT pathway of interest. This work builds on these contributions by also highlighting the value in assessing "undesired" CT pathways by inspecting the other "routes" the signal follows throughout a phase cycled experiment.

Thus, the domain colored coherence transfer (DCCT) schema aids in diagnosing instrumental shortcomings, and in the applications outlined here, it has also proven useful for elucidating signals in systems and experiments that previously precluded standard ODNP analysis, thus widening the expanse of ODNP applications. More broadly, the DCCT schema should benefit not only ODNP but also other MR methods, such as pulse EPR, 32-34 well-logging, 35 and process monitoring, 36 and more generally other forms of spectroscopy capable of accessing multiple different coherence pathways. 37-40

This paper is organized as follows: Sec. II covers the theoretical basis of this paper, including some review, with emphasis on the mathematical basis of phase cycling (Sec. II A 1). Section II A introduces the approach to data processing and rationalizes echo detection as yielding the benefits of the EXORCYCLE,²³ while permitting routine baseline-free spectral acquisition with accurate integrals (Sec. II A 2) and phase corrections (Secs. II A 3 and II A 4). Next, Sec. II A presents the mathematics underlying a "signal-averaged" alignment routine (Sec. II A 6) and the specific apodization techniques (Sec. II A 5) and concludes with a review of ODNP theory (Sec. II B). Since compact scripting comprises part of the results presented here, equations are referenced against an appendix (Appendix A) that offers a glimpse at the corresponding code. Section III contains all relevant experimental details, such as sample preparation (Sec. III A). It supplies details regarding the modular low-field equipment (Sec. III B), including a variation that relies only on a few hardware components of relatively low sophistication (Sec. III B 3). It briefly discusses the custom Python software, which serves as a cornerstone of this work (Sec. III D). As novel data visualization/plotting techniques form a central component of the new approach, the results section (Sec. IV) begins with a demonstration (Secs. IV A and IV B), along with subsequent demonstrations of specific NMR experiments presented in Sec. IV C. This plotting technique proves particularly useful for experiments that rely on unsophisticated hardware, such as a "bare-bones" spectrometer made from nonspecialized equipment (Sec. IV C 1) and a modular system relying on a SpinCore PCI board transceiver (Sec. IV C 2); time-variable magnetic fields present in many low-field and portable instruments also provide an opportunity to showcase the applicability of this visualization technique (Sec. IV C 3). However, it can also (Sec. IV C 4) demonstrate the cooperative effect of several pulses and can be deployed on standard commercial instrumentation. The DCCT schema for organizing and plotting the data then motivates and facilitates the algorithms in Sec. IV D, which presents phasing (Sec. IV D 1), correlation-based frequency alignment in the presence of phase cycling at low signal-to-noise ratio (SNR) (Sec. IV D 2), and apodization (Sec. IV D 4). Collectively, these processing procedures prove extremely flexible and adaptable to the inversion recovery (Sec. SI-D) and to the progressive enhancement (Sec. IV D 3) experiments that are essential to recording data relevant to hydration dynamics. The schema proves particularly useful in a uniquely low SNR case scenario (Sec. IV D 5), which highlights the utility of this means of data handling and presentation. Secs. V and VI place the schema in the broader context of existing NMR literature and forecast future applications. Note that abbreviation DCCT refers to two key elements of the strategy presented here: (1) domain coloring for plotting the complex-valued data and (2) the formalization of CT dimensions. While the "DCCT map" refers to the colored map of the signal flowing through all coherence pathways, the "DCCT schema"

refers to the overall strategy: not only plotting of the signal map but also data organization and coding.

Overall, the techniques introduced here enable synergy between data acquisition and processing, which relies less on starting infrastructure and allows for greater sophistication in the processed results. Looking forward, the DCCT map and the resulting signal optimization techniques not only facilitate improvements in processing methodologies, such as those presented here, but also provide the framework for many future advances.

II. THEORY

A. Data processing

Several sections below utilize the notation

$$c(\Delta x) = f(x) \star g(x)$$

for the correlation function. A correlation function ultimately seeks to describe the similarity between two functions f(x) and g(x). In particular, for two similar functions f(x) and g(x), the correlation function $c(\Delta x)$ will rise to a maximum for an abscissa (Δx -value) corresponding to the x-offset between f and g. The correlation function $c(\Delta x)$ is calculated via

$$c(\Delta x) = \int_{-\infty}^{\infty} f^*(x)g(x + \Delta x)dx,$$
 (1)

in which the function g(x) on the right is displaced by some factor Δx and applied to the complex conjugate of the function (f(x)) on the left. This overlap integral produces the correlation function $c(\Delta x)$. Aside from providing compactness, this notation emphasizes the fact that a Fourier domain multiplication $(\tilde{c}(v) = \tilde{f}^*(v)\tilde{g}(v))$ significantly outperforms the numerical integration of Eq. (1).

1. Phase cycling

During the course of a pulsed NMR experiment (or indeed any coherence pulse spectroscopy), the coherences that ultimately give rise to signal can interconvert at various points during the pulse sequence. These coherences can be classified by coherence order: defined as the difference in the net quantum number between the two states summed in the quantum superposition corresponding to the relevant coherence. Equivalently, the coherence order is the distance of the coherence term from the diagonal in the matrix representation of the density matrix.

Phase cycling is a process by which the phase of the rf pulses of an NMR experiment label the generated signal with a specific phase that corresponds to the change in coherence order during a pulse. MR spectroscopists traditionally represent the "pathway" of such changes as a coherence level diagram [e.g., Fig. 3(c)]; conceptually, such "coherence transfer (CT) pathways" are analogous to "double sided Feynman diagrams" in optical and infrared spectroscopy. In the simplest example, utilized repeatedly in this work, of a spin echo, a 180° pulse converts a coherence of +1 order (corresponding to the density matrix term $|m_s = +\frac{1}{2}\rangle\langle m_s = -\frac{1}{2}|$ for orientational quantum number m_s) to a coherence of -1 order ($|m_s = -\frac{1}{2}\rangle\langle m_s = +\frac{1}{2}|$) in order to generate the signal of interest. However, this well-used formalism also extends in a straightforward way to other pulse sequences as well as to higher-order coherences relevant to multiple quantum spectroscopy.

The isolation of a particular CT pathway usually involves application of a receiver phase factor. Traditionally, the hardware implements this phase factor with each step of the phase cycle. However, the alternative approach of saving transients separately and implementing the receiver phase in post-processing is well known and likely used to various extents by different labs, especially on homebuilt NMR systems. DCCT extends and formalizes this latter approach to offer various benefits as a diagnostic and signal processing tool, as will be elaborated by the results. In particular, one can improve traditional phase cycling and use more of the measured transients to provide more signal. Key to this strategy is the following well-established principle that relates the raw phase cycled data to signals arising from the various CT pathways:

$$s(\Delta p, t) = \frac{1}{\sqrt{n_{\varphi}}} \sum_{j=0}^{n_{\varphi}-1} e^{-i2\pi \Delta p_j \varphi_j} s(\varphi_j, t), \tag{2}$$

where n_{φ} gives the number of phase cycle steps and, following standard notation, Δp_{j} indicates the coherence change during pulse j. The phase angle φ_{j} has units of [cyc] = [rad]/ 2π , such that an x-pulse has $\varphi = 0$ cyc, a y-pulse has $\varphi = 0.25$ cyc, etc.; the resulting Δp_{1} are then unitless. This article employs the phrasing that Eq. (2) relates the "phase cycling domain" (φ_{j}) to the Fourier conjugate "coherence transfer domain" (Δp_{i}).

When the pulse sequence cycles the phase of multiple pulses, the signal in the coherence transfer domain, $s(\Delta p_1, \Delta p_2, \ldots, \Delta p_N, t)$, derived from an N-dimensional Fourier transform of the phase cycling domain signal, gives the component of the signal that changes by Δp_1 during the first pulse, Δp_2 during the second pulse, etc. Thus, $s(\Delta p_1, \Delta p_2, \ldots, \Delta p_N, t)$ includes the signal for all distinguishable CT pathways, and a choice of a particular set of Δp_j values selects the signal for a particular CT pathway. The Δp dimensions are subject to standard Fourier aliasing, resulting from the Nyquist theorem. When a single coherence transfer pathway is selected, this aliasing collapses to the well-known rules laid out in the seminal phase cycling contribution from Bodenhausen, Kogler, and Ernst. 25,42

2. Deriving integrals from echoes

ODNP relies on high-quality quantitative NMR that requires properly phased signal without a baseline. The inhomogeneous fields and low SNR conditions commonly encountered in ODNP pose some obstacles toward routinely acquiring data with correct phasing that avoids baseline artifacts. Fortunately, the echo-based signal acquisition advocated in this work not only refocuses inhomogeneities but also circumvents baseline problems by recovering signal typically lost to the pulse dead time, as encountered in pulsed ESR spectroscopy, ³² thus yielding distortion-free early time points of the free induction decay (FID). ⁴³ Echo-based signal acquisition also reaps the benefits provided by the EXORCYCLE ²³ and permits straightforward automated approaches for signal phase correction. Typical 90° pulse and subsequent 180° pulse lengths are advantageously short (\leq 10 μ s) in most ODNP systems, while T_2 times are long (hundreds of ms to s), garnering these benefits virtually free of cost.

Phase correction routines identify the origin of the time axis (t = 0), defined as the time point at which all the isochromats in

the signal present the same phase. ^{43,44} For an idealized (noise-free) echo, t = 0 corresponds to the peak of the echo. Echoes symmetric about t = 0 yield purely real Fourier transforms, but echoes generated in response to short echo times (which refocus shortly after the 180° pulse) can also be converted to FIDs via multiplication by an appropriate Heaviside function, h(t),

$$s_{\text{FID}}(t) = s(t)h(t) = \begin{cases} 0, & t < 0, \\ \frac{1}{2}s(t), & t = 0, \\ s(t), & t > 0. \end{cases}$$
 (3)

Before the code implements Eq. (3), it must adjust the origin of the time axis, possibly by a nonintegral multiple of the dwell time (the time domain sampling interval). The pySpecData Python library⁴⁵ (developed in-house and used here throughout) provides a compact notation that selects and manipulates the signal based on its time coordinates (listing A.1). Upon Fourier transformation, the pySpecData library automatically generates an appropriate axis of frequency coordinates and, for time axes that do not begin at t=0, automatically multiplies in the frequency domain by the appropriate first-order phase shift.

The relatively simple treatment of short-time echoes contrasts with the behavior of FIDs arising in response to an isolated 90° pulse. Assuming the frequency domain signal comprises a superposition of Lorentzians, beginning acquisition on a time axis (t') at some time point t_d after the nominal center of the echo (s.t. $t = t' + t_d$) results in

$$\sum_{j} e^{i2\pi v_{j}t - R_{j}t} h(t - t_{d}) = \sum_{j} e^{i2\pi v_{j}t_{d}} e^{-R_{j}t_{d}} e^{i2\pi v_{j}t' - Rt'} h(t'),$$
 (4)

that is, each resonance changes slightly in amplitude and phase. Of course, in mild cases, a uniform first-order phase shift can correct for the change in phases. However, it is also known that issues arise from either distortion of the initial FID datapoints⁴³ as well as from the interference of nearby peaks (especially their dispersive components). These issues are particularly noticeable when choosing a value of t_d that is a non-integer multiple of the dwell time. 46,47 Techniques such as linear prediction (LP) and baseline correction mitigate these effects by effectively reconstructing or adjusting the values of the datapoints that comprise the early time points of an FID; in choosing a specific algorithm, and ascribing to the assumptions of that algorithm, the user effectively adjusts several free parameters corresponding to the values of the early time points of the FID. In contrast, echo detection offers a means to address this dilemma through choice of a single free parameter—the time coordinate that gives the center of the echo and the start of the FID.

3. Zeroth-order phase correction

Very simple methods for calculating the zeroth-order (frequency-independent) phase correction behave well when all peaks are positive; however, both for inversion recovery and for ODNP enhancement curves, the sign of any given peak is unknown. Therefore, given a collection of complex datapoints (s_k) assumed to be distributed primarily along the real axis of the complex plane and then rotated by some arbitrary constant (zeroth-order) phase, the principal axis of the matrix

$$I_{ij} = \sum_{k=1}^{N} \begin{bmatrix} |s_k|^2 - \text{Re}[s_k]^2 & \text{Re}[s_k]\text{Im}[s_k] \\ \text{Re}[s_k]\text{Im}[s_k] & |s_k|^2 - \text{Im}[s_k]^2 \end{bmatrix}$$

$$= \sum_{k=1}^{N} \begin{bmatrix} \text{Im}[s_k]^2 & \text{Re}[s_k]\text{Im}[s_k] \\ \text{Re}[s_k]\text{Im}[s_k] & \text{Re}[s_k]^2 \end{bmatrix}$$
(5)

(motivated by the formula for the inertia tensor) would provide the vector in the complex plane that the real axis had been rotated to. The zeroth-order phase correction that corresponds to rotating this axis to align with the real axis performs well even when the datapoints have a variable sign.

4. First-order phase correction

The expression

$$\tau_{echo} \approx \tau + 2t_{90}/\pi \tag{6}$$

provides a reasonable approximation to the actual observed τ_{echo} based on the ninety time t_{90} and inter-pulse delay τ in a spin echo experiment. However, in practice, hardware trigger delays, group delays due to line transmission, etc., collectively contribute to changing the effective position of the echo center such that the exact center position must be determined experimentally. 44,49

If the timescale of the inhomogeneous decay (T_2^*) exceeds the required timing correction, the determination of the center maximum of the echo frequently proves less trivial than expected. In particular, the presence of noise complicates attempts to choose between the amplitude of time points near the peak of the echo, where the magnitude is relatively flat as a function of time. Furthermore, echoes resulting from experiments that invert some isochromats but not others (or from antiphase signal) will not necessarily present maximum amplitude at the center of the echo.

Two strategies yield more robust procedures for finding the echo center:

The first strategy exploits the fact that the echo signal in the time domain must have Hermitian symmetry $(s(t) = s^*(-t))$. Therefore, the cross-correlation of the echo waveform with its Hermitian conjugate can identify the timing discrepancy between the instrumentally assigned time axis and the "true" time axis, where t = 0 corresponds to the echo center.

Invoking established procedure for analogous calculations in the molecular dynamics literature, 50 this strategy begins by zero-filling the signal, s(t), to twice its length. For a discrete signal with N datapoints, the resulting zero-filled signal $s_{zf}(t)$ has length $2Nt_{dw}$, where t_{dw} (the dwell time) gives the separation between datapoints in the time domain. The following equations will utilize the fact that s_{zf} (or any signal treated by a discrete Fourier transform) is mathematically modeled as infinitely repeating, with a periodicity equal to its length $(2Nt_{dw})$. For any real inhomogeneous broadening, the cost function

$$c(\Delta t) = \frac{t_{dw}}{\Delta t + t_{dw}} \int_{-\Delta t}^{0} \left| e^{i\varphi_0} s_{zf}^*(-t) - e^{-i\varphi_0} s_{zf}(t + \Delta t) \right|^2 dt \qquad (7)$$

should drop to a minimum for a value of Δt , named Δt_{\min} , that gives the time shift needed to align the echo center in $s_{zf}(t)$

with the echo center in the Hermitian conjugate $s_{zf}^*(-t)$ (bearing in mind the periodicity of both functions). Therefore, $\Delta t_{\rm min}/2$ corresponds to the difference between the original (instrumental) t=0 and the center of the echo. In Eq. (7), the integral limits run only over times where the integrand is nonzero and multiplication with the term outside the integral normalizes by the number of integrated datapoints; φ_0 signifies that the zeroth-order phasing of the signal remains unknown until the determination of the echo center. Expansion of the modulus squared yields

$$c(\Delta t) = \frac{t_{dw}}{\Delta t + t_{dw}} \left[\int_{-\Delta t}^{0} \left| s_{zf}^{*}(-t) \right|^{2} + \left| s_{zf}(t + \Delta t) \right|^{2} dt - 2 \int_{0}^{2Nt_{dw}} \Re \left[e^{-i2\varphi_{0}} s_{zf}(t + \Delta t) s_{zf}(-t) \right] dt \right],$$
 (8)

where the limits of the third term have been expanded into regions where the integrand is zero. Substitution of integration variables and utilization of the definition of the correlation symbol then yield

$$c(\Delta t) = \frac{2t_{dw}}{\Delta t + t_{dw}} \left[\int_0^{\Delta t} \left| s_{zf}(t) \right|^2 dt - \Re \left[e^{-i2\varphi_0} s_{zf}^*(-t) \star s_{zf}(t) \right] \right].$$
 (9)

Finally, note that the choice of φ_0 that will minimize the previous expression is simply the phase of $s_{zf}(t)$ at the echo center. Therefore, the expression

$$c'(\Delta t) = \frac{2t_{dw}}{\Delta t + t_{dw}} \left[\int_0^{\Delta t} |s_{zf}(t)|^2 dt - |s_{zf}^*(-t) \star s_{zf}(t)| \right]$$
(10)

has a minimum at the same Δt as Eq. (9). As the Fourier transform of the second term in Eq. (10) is the square of the Fourier transform of $s_{zf}(t)$, the Hermitian conjugate shown in the second term is never explicitly calculated.

The second phasing strategy relies on the fact that the integral of the absolute value of the absorptive component of a Lorentzian peak is smaller than the absolute value of the dispersive component. Previous literature has extensively employed this principle for first-order phase correction of FIDs.⁵¹ In the present context, this amounts to finding the minimum of the cost function

$$C(t_d) = \int \left| \Re \left[e^{-i\varphi_0} h(t - t_d) s(t) \right] \right| dt.$$
 (11)

Of course, this cost will artificially fall off as t_d is pushed to later portions of the signal decay, so we instead optimize

$$C(t_d) = \frac{\int \left| \Re \left[e^{-i\varphi_0} h(t - t_d) s(t) \right] \right| dt}{\int \left| \Im \left[e^{-i\varphi_0} h(t - t_d) s(t) \right] \right| dt}.$$
 (12)

While this cost function might be expected to fluctuate significantly at low signal energies, it can still provide useful context, especially for sequences that employ standard 90° pulses or very short echo times.

5. Linewidth and apodization

For various purposes, the spectroscopist may desire to determine a generic measure of linewidth, defined even for complicated line shapes. For low-field data, standard apodization techniques (such as Lorentzian-to-Gaussian transformations) prove useful on several fronts. Therefore, a consistent definition of standard line shapes and quantification of their signal energy $(\propto \int |s(t)|^2 dt$ = $\int |s(v)|^2 dv$) are advantageous.

The Fourier transform (with limits $\pm \infty$) of

$$s_G(t, \lambda_G) = \exp\left(-\frac{\pi^2 \lambda_G^2 t^2}{4 \ln 2}\right)$$
 (13)

is a Gaussian with full-width-half-maximum (FWHM) of λ_G , integral 1, and signal energy

$$E_G(\lambda_G) = \sqrt{\frac{2 \ln 2}{\pi}} \frac{1}{\lambda_G},\tag{14}$$

while the Fourier transform of

$$s_L(t,\lambda_L) = \exp(-\pi\lambda_L|t|)$$
 (15)

is a Lorentzian with FWHM of λ_L , integral 1, and signal energy

$$E_L(\lambda_L) = \frac{1}{\pi \lambda_L}. (16)$$

The preceding statements are true for spin echo signal that includes both a rising refocusing period as well as a decay. Signal comprising exclusively a perfect FID [Eq. (3)] would yield an integral with half the size and an energy of half the magnitude.

Apodization requires some knowledge of the original experimental linewidth for optimal results. However, the presence of inhomogeneities can complicate the definition of such a linewidth. A fairly robust strategy for determining the generalized linewidth can be adopted from a strategy of fitting the envelope (the sum of the absolute value of the time domain waveform along any indirect dimension) of the time domain waveform to either a Gaussian or decaying exponential function. The folded normal distribution 52 gives the functional form of the time domain signal envelope as y'(t),

$$y'(t) = \sigma_n \sqrt{\frac{2}{\pi}} \exp\left(-\frac{A^2 y(t)^2}{2\sigma_n^2}\right) + Ay(t) \operatorname{erf}\left(\frac{Ay(t)}{\sqrt{2\sigma_n^2}}\right), \quad (17)$$

where y(t) is either Eq. (13) or Eq. (15), σ_n is the standard deviation of the instrumental noise, and A is the signal amplitude.

Finally, when considering the Lorentzian-to-Gaussian transformation, a range of final linewidths could be chosen, with narrower linewidths reducing the SNR. This article will consider two cases. First, when SNR considerations are significant, it is sensible to choose the λ_G of the resulting (output) Gaussian to be of equal integral and energy to the Lorentzian of intrinsic linewidth λ_L . Specifically, this corresponds to $\lambda_G = \lambda_L \sqrt{2\pi \ln 2}$, for which $E_G(\lambda_G) = E_L(\lambda_L)$, and, overall, an apodization operation of

$$s'(t) = s(t) \exp\left(\left(-\frac{\pi^2 \lambda_L t^2}{2} + |t|\right) \pi \lambda_L\right), \tag{18}$$

where λ_L comes from the generic linewidth determined from the signal envelope. In the second case,

$$s'(t) = s(t) \exp\left(\left(-\frac{\pi \lambda_L t^2}{4 \ln(2)} + |t|\right) \pi \lambda_L\right)$$
 (19)

implements an equal linewidth transformation, replacing a Lorentzian of λ_L with a Gaussian of the same FWHM.

6. Alignment by cross-correlation

Field fluctuations of permanent magnets and room temperature electromagnets lead to slight shifts in the resonance frequencies of subsequent transients. In some cases, field drift may even be present in high resolution superconducting magnets, such as during MAS experiments, and can be dealt with by applying a linear phase correction to the data acquired in reasonable time blocks.⁵³ Some previous methods for spectral alignment have relied on iterative Bayesian⁵⁴ or other statistical means to align signal,⁵⁵ while others invoke correlation of spectral fragments. 56,5 These methods typically operate on the absolute value of the signal or well-phased signal, have not been implemented for low-field signal, or do not allow for independent shifting of phase cycled transients. More recent studies have demonstrated the promise of cross-correlation of transients as a simple and potent technique to align NMR transients in the presence of a variable field in low-field systems. 19,58 In fact, cross-correlation can explicitly deal with complex signals undergoing phase cycling and can be clearly mathematically justified. Motivated by this, we introduce a specific variant of cross-correlation (signal-averaged mean-field cross-correlation) that can function even under circumstances where individual pairs of transients do not offer sufficient SNR for alignment.

Consider inspecting the signal from two transients in the frequency domain, $S_j(\nu)$ and $S_m(\nu)$, shifting S_j to the left by $\Delta \nu_j$ to maximize the norm of the resulting signal $|S_m(\nu) + S_j(\nu + \Delta \nu_j)|^2$ —i.e., consider maximizing the expression

$$\int |S_{m}(v) + S_{j}(v + \Delta v_{j})|^{2} dv = \int |S_{m}(v)|^{2} dv + \int |S_{j}(v + \Delta v_{j})|^{2} dv + 2 \int \Re[S_{m}^{*}(v)S_{j}(v + \Delta v)] dv, \quad (20)$$

where S_j and S_k are periodic (because Fourier transformation of discretely sampled time domain signals generates periodic frequency domain signals).

Therefore, not only the first term in Eq. (20), but also the second term, remains constant for all values of Δv_j . Consequently, the problem of aligning the signals in the frequency domain to give maximum overlap mathematically corresponds *exactly* to the much simpler problem of finding the maximum of the real part of the correlation function $(C(v_j))$ in the third term, where

$$C(\Delta v_j) = \int S_m^*(v) S_j(v + \Delta v_j) dv$$

= $S_m(v) \star S_j(v)$ (21)

and where the second equality makes use of the \star symbol [Eq. (1)], and the FFT makes calculation trivial and fast. Difficulties in applying this mathematical truism to real data appear when considering noise and phase cycling.

As implicitly recognized in previous literature, 57 note that Eq. (21) integrates over regions of ν that potentially contain exclusively noise. Noisy transients will lead to noisy correlation functions, meaning the position of the maximum of Eq. (20) will be influenced by the maximum of the signal and the presence of noise. This effect will degrade SNR of the correlation function even for values of $\Delta \nu$ that correspond to well-aligned signal, making it important to leave out frequencies that contain only noise.

Even then, a single transient may not provide sufficient SNR to even identify the presence or absence of signal. Importantly, the generalization of Eq. (21) to the case of more than two transients involves the consideration of not only the overlap of adjacent transients, but also the total overlap of all transients, and requires finding the maximum of the real part of

$$C(\Delta v_1, \dots, \Delta v_J) = \sum_{\substack{m,j \\ m \neq j}} \int S_m^* (v + \Delta v_m) S_j (v + \Delta v_j) dv$$
$$= \sum_{\substack{m,j \\ m \neq j}} S_m (v + \Delta v_m) * S_j (v)$$
(22)

to determine the corrective shifts in an experiment with J transients. Note that Eq. (22) depends on the shifts for all transients, simultaneously; thus, the ellipsis indicates the presence of J arguments to the highly multidimensional function C, while the sum varies m and j across all possible combinations of the J transients. The approach to optimizing C adopted here involves finding a "mean field"-type solution that fixes all but one of the Δv_i ,

$$C_{mf.}(\Delta v_j) = \sum_{\substack{m \\ m \neq j}} \Re[S_m(v) \star S_j(v)], \tag{23}$$

where the correlation resulting from \star is a function of Δv_j [Eq. (1)], with the position of all other transients [Δv_m in Eq. (22)] held constant. This expression generates a single one-dimensional curve for each transient (of subscript j), each of which yields a clear optimal Δv_j . This solution requires iterating until the list of $\Delta v_j \rightarrow \Delta v_m$ values remains consistent from one iteration to the next: typically 3–10 iterations. While requiring a more laborious computation by demanding calculation of all possible correlation functions between all possible transients (rather than merely, e.g., adjacent transients in a time series), the sum in this expression actually involves a signal averaging of the correlation function and proves particularly important in the case where individual transients may have particularly low SNR. We, therefore, refer to Eq. (23) and its generalization to phase cycled signal, below, as a "signal-averaged correlation function."

Aligning in the presence of a phase cycle comprises the second main consideration here. Following the DCCT schema, one can treat phase cycling as an added dimension, Fourier transform into the coherence domain, and then seek to optimize the portion of the (Frobenius) norm of the signal that varies with the frequency shift. The norm squared is

$$C(\Delta \nu_{1,1}, \dots, \Delta \nu_{J,K}) = \sum_{l} \int \left| \sum_{j,k} e^{-i2\pi \varphi_k \Delta p_l} \right|^2 dv$$

$$\times s_{j,k} (\nu + \Delta \nu_{j,k}, \varphi_k) \Big|^2 dv$$
(24)

for an experiment with J repeated scans cycled over K phases. Here, the sum over j spans all signal-averaged repeated scans, while the sum over k spans all pulse phases and the sum over l spans all coherence transfer values. Again (as indicated by the ellipsis), C is highly multidimensional. As in the 1D case, one could consider optimizing C by iteratively optimizing the individual mean-field correlation functions arising from the cross-terms (between j, k vs m, n terms) of Eq. (24) and iterating $\Delta v_{j,k} \rightarrow \Delta v_{m,n}$ to convergence. Isolating the cross-terms, analogously to Eqs. (20) and (21), and rearranging slightly yield

$$C_{m,f.}(\Delta v_{j,k}; \Delta p_l) = \Re \left\{ e^{-i2\pi\varphi_k \Delta p_l} \sum_n e^{+i2\pi\varphi_n \Delta p_l} \right.$$

$$\times \sum_{\substack{m \\ m \neq j}} \int \left[s_{m,n}^*(v, \varphi_n) \right.$$

$$\times s_{j,k}(v + \Delta v_{j,k}, \varphi_k) \left] dv \right\}. \tag{25}$$

The cross-terms of Eq. (24) involve summing $C_{m.f.}$ over all values of Δp_l ; however, as rationalized later, the code will frequently only calculate $C_{m.f.}(\Delta v_{j,k}; \Delta p_l)$ for a subset of Δp_l values, so Eq. (25) will prove more convenient. After defining $\Delta \varphi_n = \varphi_k - \varphi_n$, rearranging the summations, and taking advantage of the \star symbol (now redefined to generate a function of $\Delta v_{i,k}$), this becomes

$$C_{m.f.}(\Delta v_{j,k}; \Delta p_l) = \sum_{n} \Re \left\{ \sum_{\substack{m \\ m \neq j}} \left[\sum_{n} \left[e^{-i2\pi \Delta \varphi_n \Delta p_l} s_{m,n} (\nu, \varphi_k - \Delta \varphi_n) \right] \right] \right.$$

$$\star s_{j,k}(\nu, \varphi_k) \right] \right\}. \tag{26}$$

Note that the code that implements the innermost sum first introduces a new dimension $(\Delta \varphi_n)$ with the same size and coordinates as both φ_n and φ_k and along which the elements of the signal are duplicated and then cyclically permuted (rolled) along the φ_{k} dimension by the index n. It then FFTs along the new $\Delta \varphi_n$ dimension. For example, if data arise from a pulse sequence repeated over eight scans, where each scan involves cycling the phase of the pulse φ_k in four steps and $C_{m.f.}$ is only calculated for a single value of Δp_l , then Eq. (26) yields a set of $8 \times 4 = 32$ functions $C_{m.f.}(\Delta v_{j,k}; \Delta p_l)$ for the 32 transients that not only cross-correlate different transients repeated with the same pulse phases (subscripted by j) but also transients that differ only in the choice of pulse phase (subscripted by k). The maximum of the real part of each of the 32 functions indicates the frequency shift to be applied to the 32 transients. The Δp_{ij} that appears in Eq. (26) represents the difference in phase between the two functions that are being correlated; the choice of Δp_i uses Δp_i to determine whether the phase term in Eq. (26) leads to addition, subtraction, or quadrature addition of the different contributions that sum to yield the correlation function.

Importantly, since the signals are periodic, Plancherel's theorem implies that different frequency shifts applied to different spectra along an indirect dimension cannot change the norm of the data. Therefore, unlike the case of frequency shifts among transients that are signal averaged [the j or m indices in Eqs. (23) and (25)], differences between the frequency shifts along the phase cycling dimension (the k or n indices) cannot lead to optimization of Eq. (24).

Both the specifics of this effect and a workaround can be considered with the simplest possible example: signal acquired with two transients under a two-step phase cycle, as exemplified in Fig. 1. Specifically, consider an idealized resonance, arising from an FID, of FWHM λ_L ,

$$s(\nu,\varphi) = \left(\frac{e^{i\varphi}}{\sqrt{2}}\right) \frac{\pi \lambda_L}{i2\pi(\nu - \nu_0) + \pi \lambda_L}$$
 (27)

acquired with $\varphi = 0$ rad and $\varphi = \pi$ rad (i.e., using a two-step phase cycle resulting in two separate transients). Upon discrete Fourier transformation (dimension of length 2) along φ into the conjugate domain Δp , the signal ($\Delta p = -1$, aliased to $\Delta p = +1$) appears centered about ν_0 at $\Delta p = +1$ [dashed red lines in Fig. 1(a)]. Such

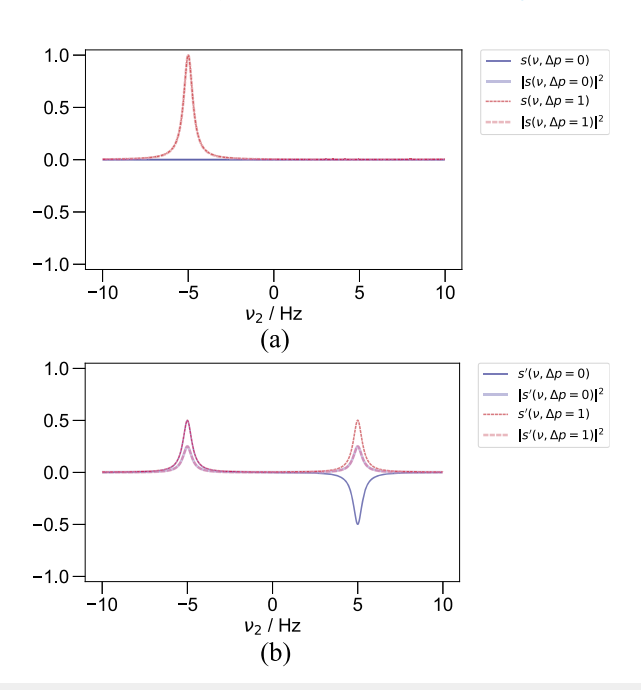


FIG. 1. A Lorentzian peak, following Eq. (27) with $\lambda_L=2/\pi$, illustrates the simplest example of how field fluctuations (typically present in low-field data) impact phase cycled data and offers insight into a method of alignment. The resonance frequency remains fixed at -5 Hz for both steps of the phase cycle in (a), while the resonance frequency for the two steps of the phase cycle is set to -5 and +5 Hz, respectively, in (b), simulating misaligned data. Dashed red represents the desired coherence pathway ($\Delta p = +1$) and solid blue represents the undesired pathway ($\Delta p = 0$). The bolder lines show the data's magnitude squared, and, for the choice of $\lambda_L = 2/\pi$, the energy of the peak (the area under the magnitude squared) is equal to the peak height. The line shapes plotted here emphasize that the overall signal energy of the data remains preserved, whether the data are aligned or not, even though misalignment spreads signal intensity over a wider bandwidth in both the frequency (ν) and coherence (Δp) domains.

a signal, with $\lambda_L = 2/\pi$, has a signal energy (norm squared) of 1, both before and after unitary Fourier transformation along the φ dimension. For this idealized signal, no signal appears in the other coherence pathway [$\Delta p = 0$; blue lines in Fig. 1(a)]. In the case where field fluctuations shift one of the transients by $\Delta v \gg \lambda_L$ [Fig. 1(b)], one transient presents signal centered at v_0 and another at $v_0 + \Delta v$. The signal must still have a signal energy of 1, so that after Fourier transformation from φ to Δp , when the signal energy from both peaks $(v_0 \text{ vs } v_0 + \Delta v)$ spreads equally across $\Delta p = 0$ and $\Delta p = 1$, and breaks into four peaks, each has a signal energy of 0.25, as shown in Fig. 1(b). Notably, misalignment spreads the signal energy both along the frequency domain (v) and the coherence domain (Δp) . This effect will also appear, to a less dramatic extent, in experimental data (e.g., Figs. SI-3 and 12).

A different signal metric-specifically a "masked norm" -provides an analog of Eq. (24),

$$N'(\Delta v_{1,1}, \dots, \Delta v_{J,K}) = \sum_{l} \int f_{mask}(v, \Delta p_{l}) \times \left| \sum_{j,k} e^{-i2\pi \varphi_{k} \Delta p_{l}} s_{j,k}(v + \Delta v_{j,k}, \varphi_{k}) \right|^{2} dv, \quad (28)$$

where the new function $f_{mask}(v, \Delta p_l)$ is the (real and positive) "mask" function. With an appropriate choice of the mask function, the masked norm N' will indeed only rise to a maximum for the choice of $\Delta v_{i,k}$ that aligns the transients.

For instance, consider a mask function that is uniform along Δp and significantly exceeds 0 along ν only in a bandwidth of similar size to the linewidth. In the example of Eq. (28), only two of the four peaks observed in Fig. 1(b)—each peak with an energy of 0.25—would contribute to the calculated masked norm. Thus, the masked norm for the properly aligned signal (\sim 1) would exhibit \sim 2× greater energy than that of the masked norm for the unaligned signal (~0.5). Attempting to optimize $N'(\Delta v_{i,k})$ for this choice of f_{mask} therefore would result in aligned signal. Considering f_{mask} of opposite construction—this time uniform along v and only nonzero for $\Delta p_1 = +1$ [the expected coherence pathway of Eq. (27)]—would lead to a similar optimization. Meanwhile, a f_{mask} selective along both Δp and ν would lead to a 4× greater energy of the masked norm for the aligned signal relative to the energy of the unaligned signal—i.e., a fourfold preference for aligned signal over unaligned signal.

Thus, to align signal in the presence of phase cycling, one should construct a $f_{mask}(v, \Delta p_1)$ that is nonzero along v only over a bandwidth similar to that of the signal and nonzero along Δp_1 only for values of Δp_1 where the signal or significant artifacts appear. Then, one can iteratively optimize the masked version of the 2D mean-field correlation function shown in Eq. (26),

$$C'_{mf.}(\Delta v_{j,k}; \Delta p_l) = \sum_{\substack{m \\ m \neq j}} \Re \left\{ \sum_{n} \left[f_{mask}(v, \Delta p_l) \right] \times e^{-i2\pi\Delta \varphi_n \Delta p_l} s_{m,n}(v, \varphi_k - \Delta \varphi_n) \right\}$$

$$\star s_{j,k}(v, \varphi_k) , \qquad (29)$$

where, as before, the \star operation operates along the ν domain to yield a function of $\Delta v_{j,k}$ (and not v) and $s_{j,k}$ is a function of three variables: v, φ_k , and $\Delta \varphi_n$. In comparing to other alignment methods, note that while the mask can and does serve as a type of "reference spectrum" for the alignment, the signal-averaged correlation function still drives alignment of the spectra; in fact, the two operate cooperatively, with the mask helping to improve the signal-to-noise ratio (via filtering) of the correlation function and the signal-averaged correlation function driving alignment of the sharper features of the spectrum.

B. ODNP

An ODNP experiment simultaneously excites ESR with microwave (µw) radiation and detects NMR with rf. It analyzes the mobility of water and discriminates motion at the timescale of the NMR resonance (here ~15 MHz) from motion at the timescale of the ESR resonance (\sim 9.8 GHz). Two different relaxivities, k_{low} and k_{σ} [M⁻¹ s⁻¹], sample the nuclear spin single-flips and the cross-relaxation between the unpaired electron and the nuclei,

Some of the experiments reported here measure the signal intensity, I(p), as a function of microwave power, p, where I(0)gives the thermally polarized (i.e., Boltzmann, non-hyperpolarized) signal intensity. The results follow the established convention³ of defining the transferred polarization as $\varepsilon(p) = (I(0) - I(p))/I(0)$,

$$\varepsilon(p) = \left(\frac{s(p)}{R_1(p)}\right) k_{\sigma} C_{SL} \left|\frac{\omega_e}{\omega_H}\right|,\tag{30}$$

where s(p) is the electron spin saturation factor (averaged across all hyperfine transitions) as a function of microwave power, $R_1(p)$ [s⁻¹] is the longitudinal relaxation rate of the ¹H nuclei as a function of microwave power, ω_e [rad/s] is the Larmor frequency of the electron, ω_H [rad/s] is the Larmor frequency of the ¹H nucleus, with, e.g., $|\omega_e/\omega_H| = 659.33 \pm 0.05$ for TEMPOL in aqueous solution.²

Importantly, minuscule variations in temperature can significantly change $R_1(p)$, thus affecting the overall $\varepsilon(p)$.² For this reason, ODNP measurements of dynamics depend on efficient $R_1(p)$ measurements to enable accurate quantification of the product of the cross-relaxivity (k_{σ}) and the saturation factor,

$$k_{\sigma}s(p) = \frac{\varepsilon(p)R_1(p)}{C_{SL}} \left| \frac{\omega_H}{\omega_e} \right|. \tag{31}$$

Equation (31) typically follows an asymptotic form, even when $\varepsilon(p)$ 59 $R_1(p)$ is found from inversion recovery experiments at different powers by fitting each set of data to the equation

$$M(\tau) = M_{\infty} (1 - (2 - e^{-WR_1})e^{-\tau R_1}),$$
 (32)

where τ represents the variable delays used in each inversion recovery experiment and W represents the magnetization recovery time. 60 Therefore, the typical procedure for ODNP entails collecting several individual NMR experiments: a series of 1D NMR spectra, recorded at different microwave powers to obtain a progressive enhancement $(E(p) = 1 - \varepsilon(p))$ curve, and also several inversion recovery experiments, recorded at different microwave powers to obtain $R_1(p)$. This article does not focus on the determination of k_{σ} for particular samples but on the acquisition of progressive enhancement and relaxation curves themselves.

III. EXPERIMENTAL

A. Sample preparation

The spin probe TEMPOL (4-hydroxy-2,2,6,6-tetramethylpiperidin-1-oxyl, Sigma-Aldrich) provides the unpaired electron for all ODNP measurements shown here, including several studies that utilize pure solutions of the spin probe in water and in toluene (Sigma-Aldrich).

For reverse micelle measurements, CTAB (hexadecyltrimethy-lammonium bromide, 0.186 g, 57 mM, Sigma-Aldrich) was dissolved in 8.39 ml of CCl₄, into which hexanol co-surfactant (0.460 g, 502 mM) was added. After addition of water (68 mg, 424 mM), a total H₂O:CTAB:hexanol ratio of 7.45:1:8.82 was obtained. The sample was then vortexed 2 × 30 s, allowed to rest for 5 min at RT, and loaded into a 0.6 × 0.8 mm² capillary tube (Fiber Optic Center, New Bedford, MA, USA) that was flame-sealed at both ends. The data for this sample were zero-filled and apodized.

For measurements of water samples not requiring ODNP, a 13 mM NiSO4 (Fisher) solution was prepared and experiments were conducted a 0.35 T.

B. Spectrometer with minimalistic, modular design

Most data were acquired on a modular NMR spectrometer operating in tandem with a Bridge12 microwave power source and the magnet of a Bruker E500 cw EPR with SuperX bridge. The modular design of the system makes several different configurations possible.

1. ODNP configuration and probe

The most frequently used configuration employs a homebuilt probe (4.8 μ l sample volume, 17 mm length) that integrates specifically with the Bruker Super High Sensitivity Probehead X-Band resonator (ER 4122 SHQE). A SpinCore RadioProcessor-G transceiver (a TTL and rf waveform generator and rf digitizer), packaged as a PCI board, interfaces with the probe by way of a homebuilt passive duplexer and standard LNA receiving chain, as well as a SpinCore rf amplifier powered by generic power supply electronics. Typical 90° pulse lengths with this setup are 4.5 μ s. Data are typically acquired with 3994 points at 1.9 kHz for a four-step phase cycle or 1946 points at 3.9 kHz for an eight-step phase cycle.

2. Large sample 15 MHz probe

Some experiments that do not require high-power microwaves instead utilize a probe with a solenoid coil rather than the typical hairpin loop employed in the ODNP experiments. In this article, these are limited to spin echo and nutation measurements. The solenoid probe, enclosed in a shielding box, accommodates a sample size of 390 μ l (approximate sample height of 20 mm in a 5 mm o.d. NMR tube), allowing for better signal-to-noise ratio. Notably, however, the larger sample size also leads to significantly larger field inhomogeneities when placed in the same location (within the EPR magnet gap) as the ODNP probe. Typical 90° pulse lengths with this probe are 7 μ s. Although this probe could prove useful for measuring relaxation times such as T_1 , the larger field inhomogeneities at the sample position relative to those of our smaller sample probes may potentially complicate these measurements.

3. NMR spectrometer independent of microwave electronics

A simple off-the-shelf oscilloscope and arbitrary waveform generator can function as an alternative to the SpinCore transceiver board. The GW-Instek AFG-2225 waveform generator generates the pulse waveforms that are amplified by an ENI 3100L RF amplifier (does not require de-blanking), while the GW-Instek GDS-3254 oscilloscope digitizes the signal after passing through an analog lowpass filter (MiniCircuits SLP-21.4+). Both the bandwidth (250 MHz) and sampling rate (5 GSPS) of the oscilloscope exceed the bandwidth of the low-pass filter.

In practice, this article was used before the SpinCore for setup and diagnostic purposes during spectrometer setup and configuration. Its inclusion in this article is for demonstration purposes, illustrating the utility of the DCCT schema on different systems. While this low cost setup is not capable of sophisticated NMR experiments that may be attainable through, e.g., an FPGA-based board, it is also less sophisticated in setup and implementation, not requiring the need to source various parts or install different libraries, implement custom PC board designs, or flash custom firmware.

C. Commercial high-field NMR

A high-field Bruker AVANCE III HD spectrometer, equipped with a broadband room temperature SMART probe with Z-gradient, acquired the high-field NMR data. By default, phase cycling on a Bruker spectrometer results in the selection of only a single coherence pathway. Thus, to implement the DCCT schema on these high-field systems, we follow the template provided in listing A.2, which saves all transients of a phase cycle.

D. Software strategy

The pySpecData library, developed in part for this work, plays a crucial role in the software strategy deployed here. Aside from storing data in an object-oriented format (with a structure not dissimilar to the xarray library⁶¹), pySpecData offers key advantages for spectroscopic data.

As a specifically relevant example, most of the methods presented here require treatment of the phase cycle as an additional dimension of the data, beyond the standard direct and indirect dimensions. To avoid confusion tracking the meaning of the multiple dimensions (e.g., whether the 1st, 2nd, or 5th dimension encodes phase cycling at a particular point in the code), pySpecData utilizes modern object-oriented capabilities. Specifically, the class of objects designed for storage of data includes a "label," along with optional units and axis coordinates, associated with each dimension. It also incorporates methods for addressing and selecting the data with compact notation and for performing common operations such as Fourier transformation. As a result, relabeling a time axis (such as centering an echo about t = 0) automatically leads to an appropriate frequency-dependent phase shift upon Fourier transformation. It also enables automatic dimensional alignment and creation that facilitates, e.g., vectorized computation of cost functions by easily introducing new dimensions corresponding to different choices of optimization parameters. Other benefits include (1) uniform storage and processing of data both from proprietary file formats and directly acquired from instruments, (2) automatic interpretation of symbolic functions supplied for fitting (including the identification of fitting parameters vs data coordinates), and (3) automatic propagation of errors. An important observation reported here is that the spectroscopist can capitalize not just on the object-oriented organization of data and associated information but also on the more singularly object-oriented capabilities of the Python programming language such as operator overloading and property definitions.

Note that the term "untreated data" and "untreated signal" will be used throughout the manuscript to refer either to the time domain data as detected on the spectrometer or to the Fourier transform (frequency domain form) of these data. The domain under consideration (phase cycling vs coherence transfer, time vs frequency) will be specified with each usage. For the back-end Fourier transform algorithm, pySpecData calls on scipy,⁶² which performs either a DFT or FFT as required by the number of samples in the signal length.

IV. RESULTS

While advancing the ODNP methodology, the authors noted a need for a sweeping reevaluation of basic elements of NMR acquisition and data processing along several fronts. Although various ad hoc solutions have been developed over the years, this work focuses on addressing the lack of a consistent, modern, and wellexplained schema (approach, plan, and organization) for presenting and optimally processing all the untreated data acquired during an ODNP experiment (and, more generally, NMR techniques under active development). Conceptually, this strategy for data manipulation and visualization integrates the synergistic benefits of three techniques: (1) domain coloring for visualizing complex data,63 which removes the need for phase correction before data can be interpreted, (2) object-oriented capabilities that facilitate the treatment of new dimensions introduced to store all the information in a phase cycled experiment as well as Fourier transform operations, and (3) open-source libraries that aid in visualization.

In the following text, Sec. IV A first demonstrates how domain coloring can provide a compact representation of NMR signal phase. Formal implementation of "phase cycling dimensions" as additional dimensions in an NMR dataset yields a variety of benefits, starting with the rapid setup and optimization of the NMR experiment and instrumentation (Sec. IV C 1). A visualization of standard nutation curve data provides a straightforward introduction to this nonstandard plotting technique (Sec. IV C 2). Notably, a simultaneous presentation of all (distinguishable) coherence transfer pathways, which typically have different signal phases or timings, in a domain colored format proves surprisingly useful. We refer to the resulting image as a "DCCT map," alluding to the term "CT map" in the seminal literature.²⁵ While traditional techniques involve throwing out at least some data (undesired CT pathways, the imaginary part of data, etc.), DCCT maps provide a comprehensive overview of all acquired data in one image, visualizing the relationship between signal in the desired coherence pathway and correctly separated artifacts, as well as signal improperly sorted into undesired CT pathways. This article refers to these three contributions, respectively, as "desired signal" or "desired pathways," "artifacts" or "artifactual pathways," (Sec. IV C) and "phase cycling noise" (Sec. IV C 3). In the results that follow, DCCT maps enrich signal analysis to inform experimental design and the development of data processing algorithms (Sec. IV D), without adding any additional time cost to a more traditionally acquired NMR experiment.

A. Display of signal phase

Before considering the visualization of signal in the coherence domain, this article first tests the applicability of the domain coloring concept to untreated NMR data (i.e., data that may be Fourier transformed but without any type of phasing/timing corrections or other post-processing). Domain coloring plots appear in other fields: e.g., in solid state physics studies, hue frequently represents directionality. 64,65 Similarly, several public-domain webpages present example diagrams illustrating phase with hue. Nevertheless, such plots remain underexploited in MR data visualization. As indicated in Fig. 2(a), hue corresponds to the complex phase and value/intensity corresponds to the complex magnitude. The Matplotlib Python plotting library⁶⁸ specifically enables the development of libraries such as pySpecData to deploy a wide variety of such custom plotting styles with relative ease. Armed with this plotting technique, the spectroscopist can assess the success of an experiment at a glance, without requiring any phase or timing corrections.

A 390 μ l (Ni²⁺-doped water) sample inside the large sample solenoid coil probe provides the signal for this section. As mentioned previously, this sample size experiences a much greater range of field inhomogeneity than a probe with a capillary sample. Figure 2(b) illustrates the untreated signal (no phasing corrections, in the frequency domain), from the desired CT pathway of an echobased nutation curve (pulse sequence: θ – τ – 2θ –acq., with tip angle $\theta = \gamma B_1 p_{90}$ increasing along the indirect dimension). The inset of Fig. 2(b) shows all frequencies where the pulse excites signal while also clearly demonstrating the inversion of the signal as θ passes through 180°. During inversion, the signal passes through zero (white) while also changing color to indicate the 180° phase change (e.g., red to cyan or blue to yellow, or vice versa). A quick glance at a complex domain coloring plot can ascertain information that may otherwise require a(n) (inverse) Fourier transform and separate plot in order to be understood. For example, a time shift appears in the frequency domain plot as a "rainbow" color variation, and in the case of a spin echo, it indicates that the origin of the time axis (t = 0) does not properly align with the center of the echo signal. Here, an inspection of Fig. 2(b) (inset) indicates five cycles $(10\pi \text{ rad})$ of phase rotation over a span of 5 kHz, corresponding to a time shift of 1 ms.

Figure 2(c) introduces this 1 ms timing/phase correction, achieved by shifting the time axis (e.g.) or by applying the appropriate first-order phase shift in the frequency domain. As expected from an echo signal properly centered about t = 0, Fig. 2(c) yields a uniform phase line shape.

Figure 2 provides just one of many possible examples in which domain coloring plots both quickly guide simple manual data processing of untreated data (in the frequency domain along the direct dimension) and also allow instant access to information. Note how a real-valued plot of Fig. 2(b) would generate ambiguity between the phase variation and amplitude variation. Here, a simple glance reveals phase variation along the direct dimension and amplitude variation along the indirect dimension. Also note that information such as the time delay of the signal is accessible in both domains (time and frequency), while other plotting strategies might make this information apparent in only one domain.

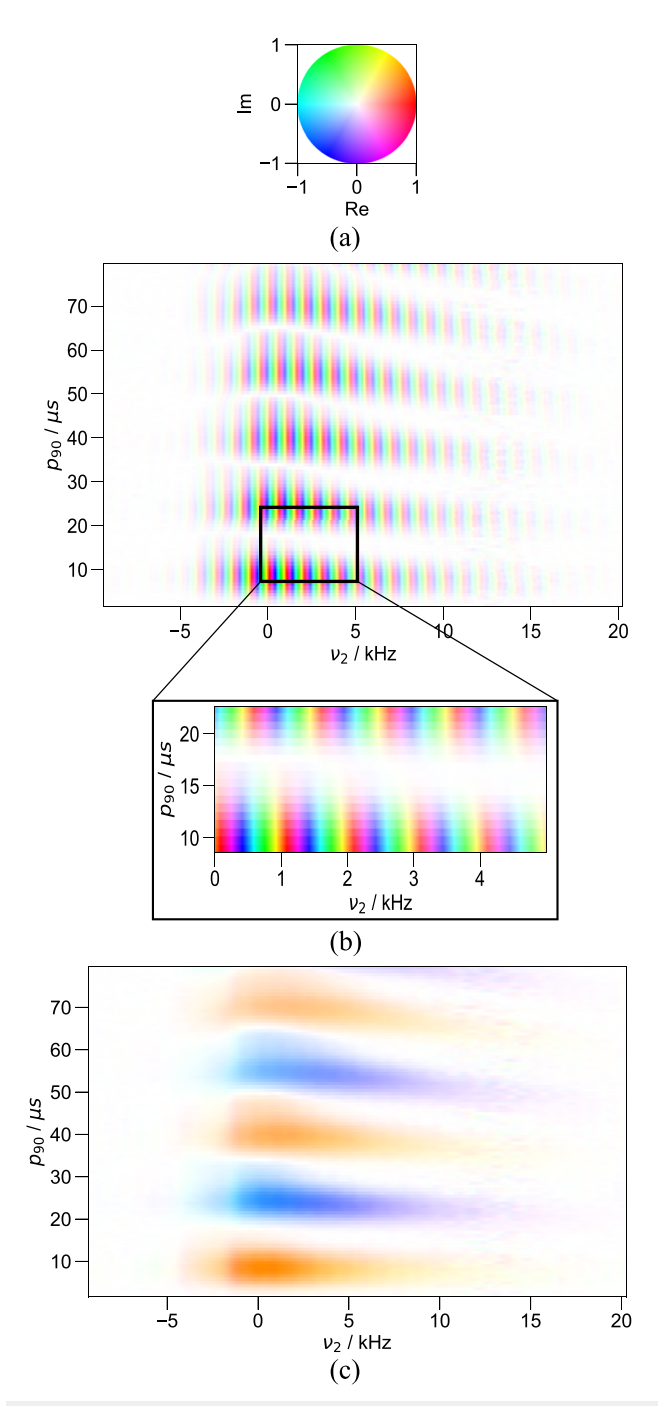


FIG. 2. (a) The coloring of data in the complex plane used in the DCCT map, where intensity indicates magnitude, and color indicates phase. (b) The untreated signal from an echo-based nutation curve after selection of the appropriate coherence pathway. Frequency-dependent phase shifts manifest in the domain coloring display as a rainbow banding (inset), here with a periodicity of 5 cyc/5 kHz = 1 ms. When zoomed out, the image may appear gray, which indicates a rapid variation in colors (phases) in the gray area. The sudden change in color from bottom to top along any particular column as the signal passes through a faint patch (amplitude near zero) indicates the inversion of the signal along the indirect dimension. (c) Application of the 1 ms time shift yields coherently phased signal.

B. Treatment of phase cycling

As demonstrated in this and the following subsections, the incorporation of many short dimensions corresponding to the cycling of individual pulses clearly illustrates the effects of drifting fields, rf amplitude misset, resonance frequency offset, and pulse ringdown. It also yields a simple scheme for quantifying the SNR ratio.

With the increased practicality offered by object-oriented programming in hand, the original conceptual approaches to phase cycling-pioneered by Wokaun, Bodenhausen, Ernst, and others—assume new meaning; these approaches incisively focus on the concept that the change in coherence order during a pulse (Δp) is quite simply the Fourier transform of the dimension along which pulse phase is cycled $[\varphi_i, \text{ Eq. (2)}]$. 25,29,69 While the traditional schema adds up the effect of all pulse phase variations to determine the overall phase cycle of the desired coherence pathway, the DCCT schema keeps matters simpler by treating each pulse involved in the phase cycle separately. To achieve this, the processing code organizes data into one or more short (typically 2-4 elements long) dimensions for each pulse involved in the phase cycling, in addition to the traditional direct (t_2) and indirect dimensions typical of multidimensional NMR experiments. Each of these phase cycling dimensions can be in the "phase cycling domain" $(\varphi_i$ for pulse i) or the conjugate "coherence transfer domain" (Δp_i) . More typical phase cycling procedures effectively filter and discard these additional dimensions. However, a central result presented here is that modern instrumentation and open-source coding⁴ standards facilitate both this treatment of the phase cycle as an additional dimension and the ability to visualize these new dimensions with automatically generated DCCT maps. Together, these offer a more comprehensive view of the underlying spin physics and of the impacts of experimental imperfections.

C. Domain colored coherence transfer (DCCT) schema

Developing new methods under adverse circumstances, such as new ODNP instrumentation or protocols, requires unambiguous identification of signal as well as quick insight into any potential issue with the setup. The DCCT map, importantly, displays the artifactual signal arising from undesired coherence pathways. Instrumental errors that lead to imperfections in the phase cycle itself can lead to miscategorization of the desired signal as arising from undesired pathways—resulting in signal loss and distortion—or miscategorization of artifactual signal as arising from the desired coherence pathway—leading to artifacts in the final result. By displaying these features, DCCT maps provide greater insight into the effects of experimental imperfections on the signal. These are most easily demonstrated through a series of examples.

1. Example: Phase cycled NMR with standard test + measurement equipment

Nonspecialized test and measurement equipment can acquire a reasonable NMR signal.⁷¹ The DCCT schema enables rapid setup and diagnosis of such "bare-bones" NMR instrumentation. For example, here, an arbitrary function generator operates as an rf source and a digital oscilloscope operates as a digital to analog converter whose bandwidth and sampling rate exceed the bandwidth of

an attached analog low-pass filter (Sec. III B 3). Such an inexpensive, uncomplicated NMR spectrometer is invaluable for diagnostic purposes—e.g., when assembling a modular ODNP spectrometer.

Object-oriented Python code⁴⁵ controls both the function generator and the oscilloscope (see listing A.4) via USB 2.0 communication, an instrumental setup similar to that which was described previously.⁷² Despite the fact that a standard oscilloscope has no built-in phase-cycling capabilities, the software can trivially save separate transients acquired with different pulse phases along with the pulse waveform as a phase reference. The object-oriented code implemented here frequency filters the results, digitally mixes down and phase references by comparison to the captured pulse waveform, and saves data in an HDF5 format. For a spin echo experiment, as in Figs. 3 and 4, it stores the data immediately available from the acquired transients in a three-dimensional array of data, with shape $n_{\varphi_1} \times n_{\varphi_2} \times n_{t_2}$, representing the function $s(\varphi_1, \varphi_2, t_2)$. Here, n_{φ_1} and n_{φ_2} are the number of phase cycling steps for the two pulses, and n_{t_2} is the number of time points along the direct dimension.

After three-dimensional Fourier transformation (without zero-filling) along the φ_1 , φ_2 , and t_2 dimensions, the signal becomes

$$\tilde{s}(\Delta p_1, \Delta p_2, \nu_2) = \iiint e^{-i2\pi(\nu_2 t_2 + \Delta p_1 \varphi_1 + \Delta p_2 \varphi_2)} \times f_{sampling}(\varphi_1, \varphi_2, t_2) s(\varphi_1, \varphi_2, t_2) d\varphi_1 d\varphi_2 dt_2,$$
(33)

where Δp_j indicates the coherence change during pulse j, v_2 gives the offset frequency (in Hz) along the direct dimension, and $f_{sampling}$ gives the function representing the instrumental and/or digital filtering and discrete sampling of the otherwise continuous signal (see SI-A for further notes). As a reminder, the coherence level change (Δp_i) and the cycled pulse phase (φ_i) are Fourier conjugates [Eqs. (2) and (33)]. A theory that treats the cycling of each pulse separately is very well established; in fact, it is the starting point for the receiver phase calculation tables found in most NMR textbooks.⁷⁴ We can take advantage of this with multidimensional object-oriented coding, as shown in listing A.5.

Figure 3 presents the DCCT map that results from an initial attempt at finding signal with a spin echo pulse sequence [Fig. 3(a)] as well as an optimized attempt [Fig. 3(b)]. In both Figs. 3(a) and 3(b), the CT pathways $\Delta p_1 = +1$ and $\Delta p_2 = -2$ contain signal unambiguously identified as arising from the spin echo. Coherence pathways that are not physically meaningful are marked with an X—e.g., in Fig. 3, the coherence order change marked by the first pulse, Δp_1 , has been marked with an X due to the fact that the initial pulse acting on polarization only generates single quantum coherence here. On the other hand, when several reasonable Δp values are Fourier aliased together, all such values are presented, separated by

In this example, the DCCT map clearly demonstrates that, despite the nonspecialized instrumentation employed here, the phase cycling of the pulses on the function generator and phase referencing of the oscilloscope operate as expected, giving clean isolation of the CT pathways. Furthermore, the sign associated with the phases can vary on different spectrometers from different manufacturers, as previously noted, 75,76 and this is observable in the DCCT map. In Fig. 3, the convention is properly applied, but an

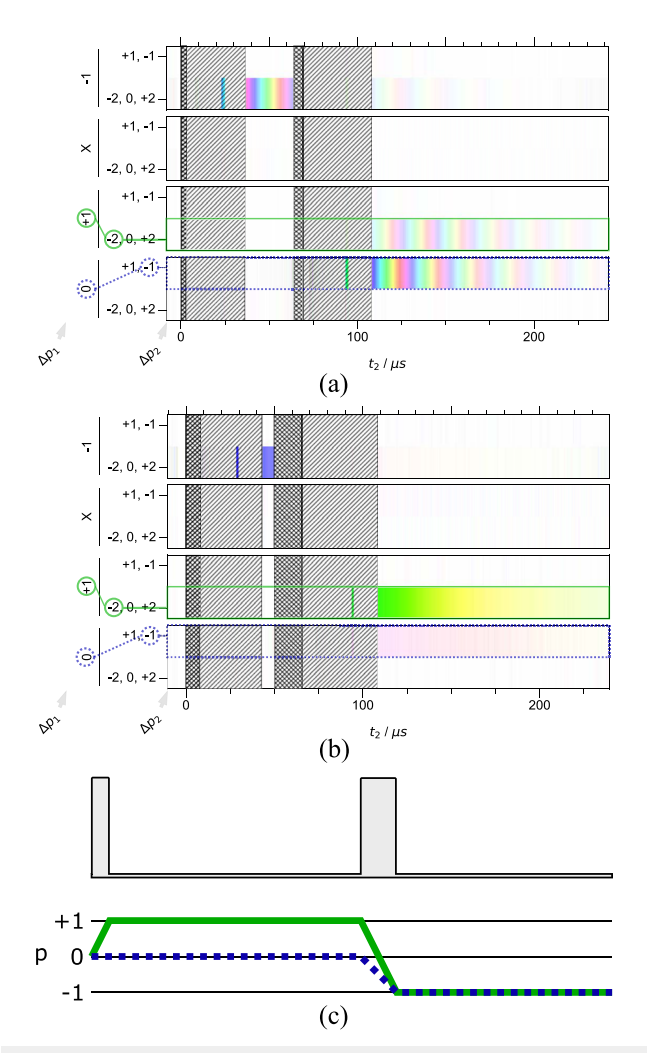


FIG. 3. Spin echo acquired by an NMR spectrometer constructed from off-the-shelf test and measurement equipment for 13 mM NiSO₄-doped water at 0.35 T (a) under suboptimal experimental parameters and (b) optimal parameters. The data distinctly peak around 120 μ s at the expected location in the coherence transfer domain—specifically, the $\Delta p_1 = +1$, $\Delta p_2 = -2$ pathway in (c), where Δp_n is the Fourier conjugate of the pulse phase (φ_n) dimension. The receiver dead time extends to ~35 μ s after the center of the 180° pulse. Low- B_1 regions of the sample contribute to the subtle signal visible at $\Delta p_1 = 0\Delta p_2 = -1$, which is an FID arising from the second pulse.

inversion of the sign of Δp (indicating an inversion of the sign of φ) could be easily observed and corrected.

Notably, Fig. 3(a) identifies that the majority of the coherences generated by the pulse sequence do not contribute to the spin echo [green solid line, Fig. 3(c)] but rather to undesired/artifactual signal, where the second, longer pulse (nominally the 180° pulse) excites an FID (p=-1) directly from the polarization (p=0) [blue dashed line, Fig. 3(c)]. The DCCT map, therefore, offers insight into experimental improvements by identifying the different pathways where the polarization has been utilized. In this simple example, after increasing the length of both pulses, the pulse sequence

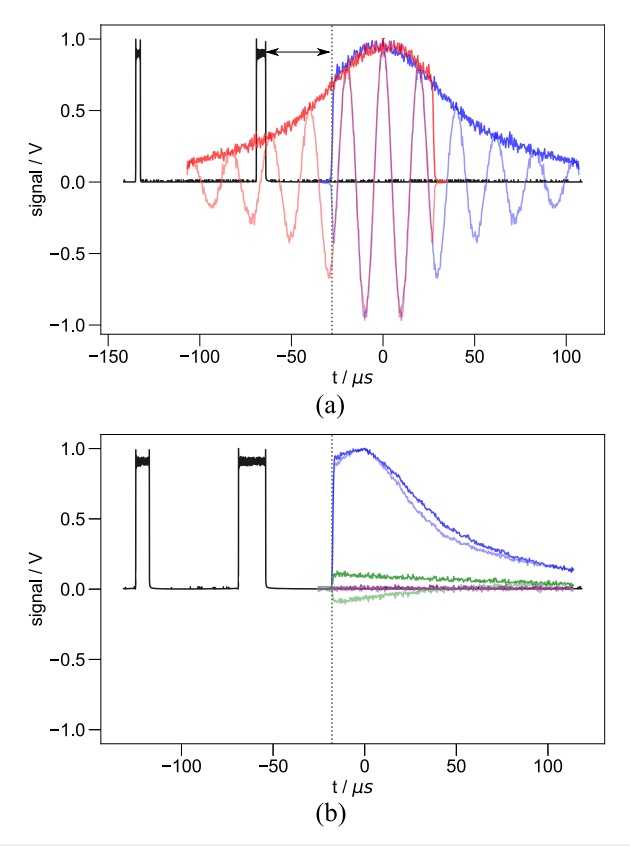


FIG. 4. (a) The subset of signal from Fig. 3(a) that follows the echo coherence pathway of Fig. 3(c) is shown, with the complex magnitude of the pulse waveform (black) and signal (blue, with the real part in fainter blue) captured by the oscilloscope shown as 1D line plots and with t=0 set to the echo center. A comparison to the Hermitian conjugate of the signal (red) clearly illustrates the time at which the signals diverge. Due to T_2^+ (inhomogeneous) decay over the timescale of the dead time (dashed black vertical line, $35.7~\mu$ s), the signal loses some 25% of its amplitude. In (b), the pulse length has been optimized and the carrier frequency set on resonance, showing the echo pathway (blue), the residual FID pathway (green), and the pathway that should not contain any signal (purple). Here, the echo pathway is much more intense than the unwanted FID pathway.

predominantly generates coherences that contribute to the spin echo signal. At the same time, the rainbow banding in the time domain data of Fig. 3(a) also indicates that the resonance frequency differs significantly from the carrier frequency. Figure 3(b) corrects both the 90-pulse time and the carrier frequency to yield an intense, single-colored band in the desired CT pathway for the echo signal.

Note that artifacts due to pulse ringdown cycle with the same phase as the pulses, in the $\Delta p=-1$ pathway for the relevant pulse, i.e., in $\Delta p_1=0 \rightarrow \Delta p_2=-1$ and $\Delta p_1=-1 \rightarrow \Delta p_2=0$. These artifacts overlay with simple (FID-like) excitation and appear here as regions of alternating signal (colored) and no signal (white), with the latter arising from times where the oscillating high-intensity ringdown saturates the duplexer diodes and/or low-noise amplifier. Thus, with a single phase cycled scan, the data can highlight how spin

echo acquisition gives uniquely unambiguous confirmation that true signal has been observed.

The DCCT schema introduces the DCCT map as an intermediate step between acquisition and presentation of the final data in a traditional phase cycled NMR experiment. The DCCT schema also opens up the possibility of other plots that display a subset of the data offered by the DCCT map, tailored to particular experiments. For example, after plotting Fig. 3, extraction of a subset of the data in a customized plot yields Fig. 4, which serves to emphasize the strong preference for echo-based detection for this large sample due to the rapid T_2^* . Meanwhile, traditional NMR acquisition employing onboard signal averaging through a phase cycled receiver would select an even more exclusive subset of the available information, detecting and saving exclusively the signal from the desired echo CT pathway $\Delta p_1 = +1 \rightarrow \Delta p_2 = -2$ [the blue line in Fig. 3(c)]; the resulting data would only indicate the presence or absence of signal.

2. Example: Nutation curve

In these results, a SpinCore RadioProcessorG replaces the USB 2.0 function generator and oscilloscope to enable faster rates of data transfer to the computer, as well as the use of digital filtering and downsampling that permit the distortionless capture of longer signals.⁷⁷

The same spin echo nutation experiment from Fig. 2 offers more information when presented as a DCCT map (Fig. 5). The full dataset comprises a four-dimensional function, $s(t_p, \varphi_1, \varphi_2, t_2)$, with a size of $n_{t_p} \times n_{\varphi_1} \times n_{\varphi_2} \times n_{t_2} = 100 \times 2 \times 2 \times 1024$. A 3D Fourier transform converts s to $\tilde{s}(t_p, \Delta p_1, \Delta p_2, v_2)$. The DCCT map demonstrates all possible conversions of the polarization to coherent signal (here both echo-like and FID-like), at all frequencies where it occurs, while simultaneously preserving all relative phase/sign information. Here, domain coloring proves crucial, given that signal from different coherence pathways occurs at different times and with different absolute phases. For example, Fig. 5 represents data from an early trial on a modular system with new components, and it was unclear if the phase cycling was functioning optimally. The DCCT map highlights the contribution of an unwanted signal artifact (blue dashed line in Fig. 5) that, in the absence of a phase cycle, would interfere with the desired signal (solid green line). It clarifies that simple hardware and data processing are capable of cleanly separating this artifact from the desired signal. Figure 5 demonstrates another general advantage of the DCCT map: The same information may be displayed and interpreted in either the time [Fig. 5(a)] or the frequency [Fig. 5(b)] domain. Specifically, note how the appearance of FID-like (blue dashed) and echo-like (green solid) signal at two different times in the time domain can be deduced directly from the rainbow banding of the FID-like signal in the frequency domain, in contrast to the constant color of the echo signal.

3. Example: Field instabilities and phase cycling noise

Another example of relevance to ODNP arises when considering field instabilities. The Bruker ESR system comes equipped with a system for generating a standard modulation field (typically varying with a period of 10 μ s), and one practical concern of ODNP spectroscopy involves what influence this might have on the NMR signal

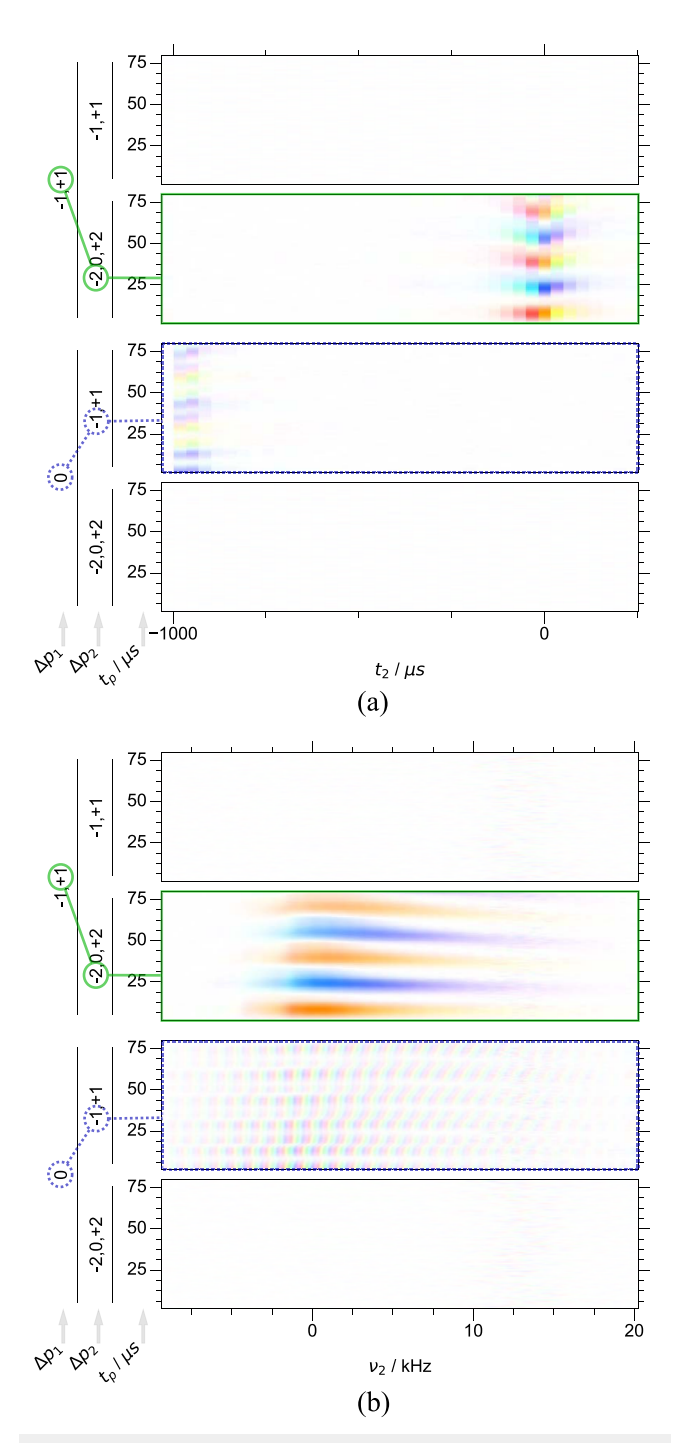


FIG. 5. Full DCCT map from a $(t_p \text{ pulse})$ - $(\tau \text{ delay})$ - $(2t_p \text{ pulse})$ sequence, where $t_p = 2$ –80 μs and $\tau = 1$ ms in both the (a) time domain and (b) frequency domain. The green boxes outline the echo CT pathway (presented exclusively in Fig. 2), while the dotted blue boxes outline the FID-like CT pathway. These pathways follow the coherence diagram outlined in Fig. 3(c) alongside the pulse sequence. The only adjustments made to the untreated data are (1) slicing to a frequency bandwidth where signal is observed and (2) setting $t_2 = 0$ to the maximum of the echo coherence pathway.

(when the spectrometer is set to "standby" mode). While a specific practical interest related to ODNP motivates this measurement, it also, more importantly, provides a controlled demonstration of general effects arising from unstable fields. The DCCT maps in Fig. 6 represent signal from a spin echo experiment comprising an 8-step phase cycle with 16 repeats, when the modulation cable is left

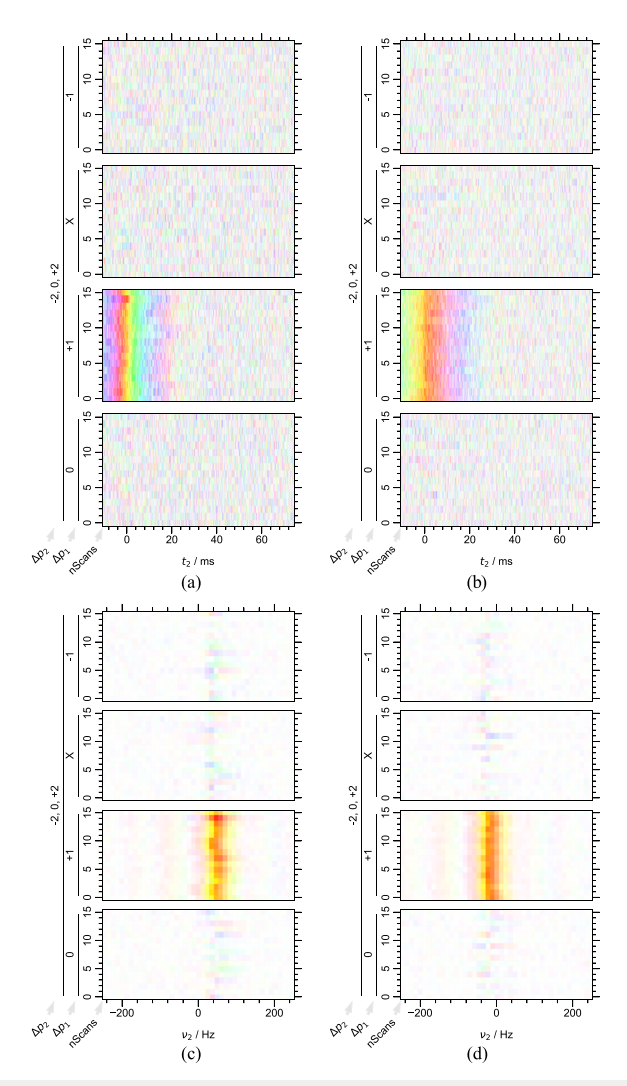


FIG. 6. Attaching vs detaching the ESR modulation coil allows for a controlled test of two situations with different field stability, as shown for both the time domain [(a) and (b)] and frequency domain [(c) and (d)], respectively. Three notable effects include the variation of the average frequency, increased amplitude of the signal in inactive coherence transfer pathways elements of the coherence dimension, and variation of the echo center. With the mod coil detached (d), the average signal value in the desired coherence pathway is $1.04\times$ that with the mod coil attached (c), while the root mean squared amplitude of the noise in all other (i.e., inactive) coherence pathways decreases by a factor of 0.86. Therefore, while the signal amplitude remains roughly equivalent, detaching the mod coil leads to a noticeable decrease in artifacts linked to improper phase cycling (variation of static field's magnitude or time dependence from one step of the phase cycle to the next).

attached to the cavity [Figs. 6(a) and 6(c)] vs when it is detached from the cavity [Figs. 6(b) and 6(d)].

The timing and phase of the echo in Figs. 6(a) and 6(b) vary from scan to scan, as evidenced by, respectively, the left vs right translation of the echo position relative to the x axis and change to the color of the signal at t=0. Notably, domain coloring helps to emphasize these concurrent variations. Again, the frequency domain DCCT maps [Figs. 6(c) and 6(d)] make the same effect evident in a different form: as changes in how the color varies from left to right across the spectrum and in the average (overall) color across the spectrum for each scan. As expected, the signal remains more stable when the connector for the modulation coil is disconnected, as in Figs. 6(b) and 6(d).

The echo signal responds to the increased field variation from the modulation coil in three specific ways. First, as already noted, the phase (color) of the signal at t = 0 (or across all frequencies) varies more across consecutive scans. This inconsistency arises from the residual modulation field driving changes in the B₀ field strength before vs after the 180° pulse. This scan-to-scan variation of the signal phase would lead to reduced signal amplitude if these scans were averaged. Second, greater frequency variation of the individual transients contributing to the signal in Fig. 6(c) [also evident from the differences in the rainbow banding of Fig. 6(a)] results in the more jagged appearance of the signal "bands" as compared to Fig. 6(d). If the various scans of Fig. 6(c) were averaged together, a distorted line shape with increased linewidth and reduced signal energy and amplitude would result, underscoring the usefulness of interrogating the impact of each transient. Third, and perhaps most significantly, in both cases, the DCCT map shows noise/artifacts in the CT pathways outside the echo-like $(\Delta p_1 = +1, \Delta p_2 = -2)$ pathway. These artifacts are concentrated within the signal bandwidth. No explanation based on the transitions between different coherence levels of the density matrix can rationalize the appearance of significant artifactual signal in these "inactive" CT pathways shown in Fig. 6. Rather, since the phase cycle must be sorting signal into the wrong CT pathway, we refer to the noise-like artifacts that appear in the inactive pathways as "phase cycling noise." The difference is subtle, but with the modulation coil detached, the noise

in the inactive channels reduces by 10% (i.e., $0.9 \times$ the noise level with the mod coil attached), as a result of a decrease in the phase cycling noise. As shown in Fig. 7, the signal intensity improves by a factor of 10% (i.e., $1.1 \times$ the noise level with the mod coil attached).

Clearly, ODNP should be acquired with the modulation coil detached under all cases. Even then, because the signal energy is diverted into energy for phase cycling noise (Sec. II A 6), the standard deviation across the coherence domain provides an appropriate source for error bars on datapoints in the spectrum. However, it will be noted that care must be taken when applying these errors to integrated signal since they can be correlated.

4. Example: CPMG

As noted in other publications, ODNP can be acquired with a CPMG (Carr-Purcell Meibloom-Gill) sequence, as is typical of many studies in low-field and portable MR. 8,10,78 An interesting result of the DCCT map arises when applied to a fully phase cycled CPMG—that is, a four-step phase cycle on a 90° excitation pulse, followed by a train of evenly spaced 180° pulses, phase cycled in concert. Some analysis schemes bin the results of the phase cycle into a "CP" component, where the phases of the 90° pulse match the phase of the 180° pulses or have a 180° phase difference, and a "CPMG" component, with orthogonal phases. Since the DCCT map offers a new means for visualizing signal, it provides the opportunity to revisit the decay of CP components and the persistence of CPMG components.⁷⁹ Briefly, following the DCCT treatment, the signal should alternate between $\Delta p_1 = +1$ and $\Delta p_1 = -1$, as in the initial echoes of Fig. 8(a); however, it starts to "bleed" into the opposite Δp_1 value following pathways like those shown in Fig. 8(b), ultimately yielding a constant signal for both values of Δp_1 . This corresponds to the previously observed decay of the "CP" component,⁷⁹ viewed from a new perspective. This example also allows the introduction of phase and coherence dimensions that group the effects of more than one pulse.

In more detail, naively following the methodology laid out in Sec. IV A, the software can sort the data into a 4D dataset

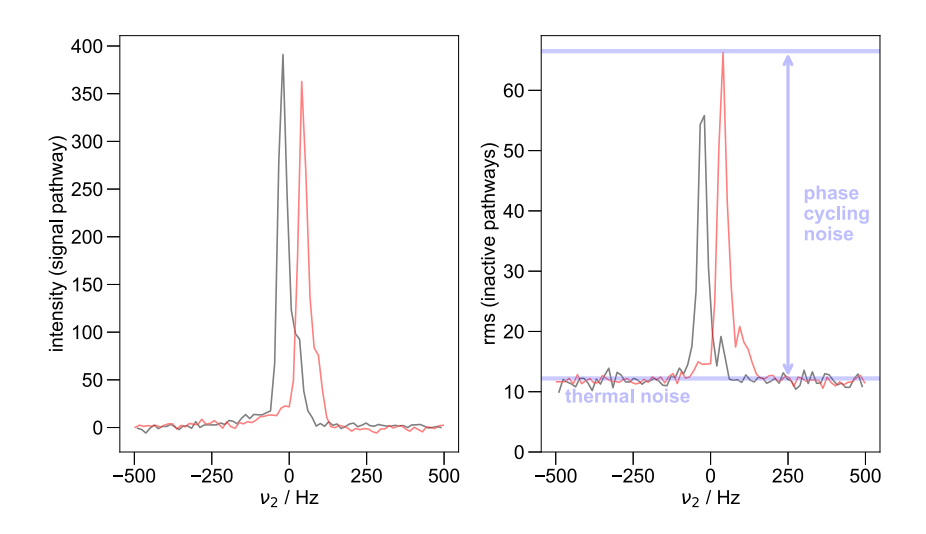


FIG. 7. The signal pathway with mod coil attached (red) exhibits weaker intensity and more complicated line shape compared to the case where the mod coil is detached (black). The averaged inactive pathways with the mod coil attached (red) demonstrate greater noise than when not attached (black): Such noise is deemed the phase cycling noise and results from phase cycling that does not function ideally. As the energy/norm of this signal comes from the shot-toshot variations of the signal, the signal amplitude (and energy) is correspondingly reduced. Removing the mod coil reduces the rms phase cycling noise by 10%.

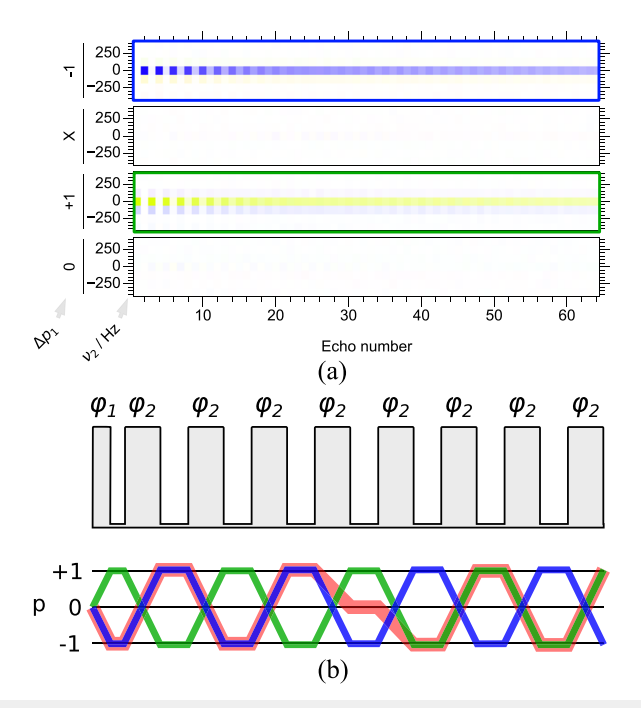


FIG. 8. DCCT map presentation of CPMG data acquired at 15 MHz with a four-step phase cycle of the initial excitation pulse (a) and an independent four-step phase cycle of all 180° pulses in concert. Here, the *x* axis corresponds to the echo number, while the direct dimension within each echo window appears as the innermost dimension along the *y*-direction. For simplicity, the single element of the $\Delta p_1 + \Delta p_2$ dimension that contains valid signal $(\Delta p_1 + \Delta p_2 = -1)$ has been selected. Detected signal alternates between two coherence pathways, viz., $\Delta p_1 = 1$, $\Delta p_1 + \Delta p_2 = -1$ (green) and $\Delta p_1 = -1$, $\Delta p_1 + \Delta p_2 = -1$ (blue), with each π pulse. Beginning with the 6th or 7th π pulse, signal "bleeding" from the alternate pathway, as shown in (b), starts to become significant. The red line gives one example of the many pathways that, cumulatively, give rise to such "bleeding."

(a single-line command in pySpecData), with the signal given by the discretized function $s(\varphi_1, \varphi_2, \tau_{echo}, t_2)$ of shape $n_{\varphi_1} \times n_{\varphi_2} \times n_{\tau_{echo}} \times n_{t_2}$, where t_2 gives the points within each echo and τ_{echo} gives the center position of each echo. It then Fourier transforms the signal along the φ_1, φ_2 , and t_2 dimensions to permit filtering by resonance frequency and coherence pathway.

The initial (nominal) 90° pulse changes the coherence order of the initial polarization by $\Delta p_1 = \pm 1$. Here, since the 180° pulses are phase cycled together, Δp_2 refers to the net change in coherence order due to all 180° pulses. Therefore, odd-numbered echoes harvest signal from the pathway that experiences $\Delta p_1 = +1$ and $\Delta p_2 = -2$. In contrast, even-numbered echoes harvest signal from the pathway that experiences $\Delta p_1 = -1$ and $\Delta p_2 = 0$.

Thus, the CPMG (Car-Purcell-Meiboom-Gill) experiment particularly motivates an informed choice of phase cycling dimensions that simplifies the analysis. Specifically, since only two types of pulses are phase cycled (along dimensions φ_1 and φ_2), a coherence-domain dimension $\Delta p_1 + \Delta p_2$ only yields signal for $\Delta p_1 + \Delta p_2 = -1$. The only signal that appears for other values of $\Delta p_1 + \Delta p_2$ arises from instrumental artifacts. A rearrangement of the expression $\Delta p_1 \varphi_1 + \Delta p_2 \varphi_2$ (which is the effect of phase cycling on the phase angle of the transients) yields

$$\Delta p_1 \varphi_1 + \Delta p_2 \varphi_2 = \Delta p_1 (\varphi_1 - \varphi_2) + (\Delta p_1 + \Delta p_2) \varphi_2 \tag{34}$$

and motivates rearranging the signal to the form $s(\varphi_1 - \varphi_2, \varphi_2, n_e, t_2)$ whose (3D) Fourier transform is given by $\tilde{s}(\Delta p_1, \Delta p_1 + \Delta p_2, n_e, v_2)$, where n_e represents the echo number.

The Δp_1 dimension disentangles the pathways that should give rise to the even vs odd echoes. Odd-numbered echoes (following 1, 3, etc., inversion pulses) should only present signal for $\Delta p_1=+1$ since the expected/desired coherence pathway with $\Delta p_1=+1$ [green line in Fig. 8(b)] only reaches p=-1 for odd echoes. Analogously, even-numbered echoes should only present signal for $\Delta p_1=-1$ [blue line in Fig. 8(b)]. The observed signal shown in the DCCT map of Fig. 8(a) derives from the alternating green and blue lines along the p=-1 coherence level. In this scheme, as long as even vs odd echoes remain separated along Δp_1 , any phase encoded between the excitation and first echo pulse would be properly preserved.

However, due to offset or misset effects, imperfect 180° pulses can store a small fraction of transverse magnetization along the z axis for one or more echo periods and then reexcite it as observable magnetization (the red pathway in Fig. 8). In Fig. 8(b), the signal cleanly separates into the desired coherence channels for the first few echoes. However, near the 7th echo, significant amounts of $\Delta p_1 = +1$ signal begin to appear in even-numbered echoes as well as significant amounts of $\Delta p_1 = -1$ signal in odd-numbered echoes—i.e., the signal "bleeds" from the even echo pathway into the odd echo pathway, and vice versa.

Figure 8(a) also demonstrates that signal from the two Δp_1 pathways can be combined into a single decay with coherent phase by subtracting (adding with a phase rotation of 180°) the $\Delta p_1 = -1$ signal and the $\Delta p_1 = +1$ signal. Such an operation reduces to

$$\frac{1}{2}(\tilde{s}(t_2,+1) - \tilde{s}(t_2,-1)) = \frac{1}{2} \sum_{n=0}^{3} \left((-i)^n s \left(t_2, \frac{n}{4} \right) - (i)^n s \left(t_2, \frac{n}{4} \right) \right) \\
= -i s \left(t_2, \frac{1}{4} \right) \\
+ i s \left(t_2, \frac{3}{4} \right), \tag{35}$$

where s is a function of t_2 and $\varphi_1-\varphi_2$, \tilde{s} is a function of t_2 and Δp_1 , and n gives the integral steps of $\varphi_1-\varphi_2=\frac{n}{4}$; moreover, the second line uses the standard identity $e^{\frac{n\pi}{2}}=i^n$ in conjunction with Eq. (2) and the third line keeps only the surviving terms of the sum. Thus, subtracting signal from the $\Delta p_1=+1$ and -1 pathways is mathematically equivalent to adding the two CPMG components $(\varphi_1-\varphi_2=\frac{1}{4},\frac{3}{4}$ cyc). Similarly, a sum of the +1 and -1 pathways—equivalent to isolating the CP $(\varphi_1-\varphi_2=0,\frac{1}{2}$ cyc) component—would cancel out the long-lived tails of the signal, which are 180° out of phase. Thus, interestingly, the "CP" vs "CPMG" components of the signal arise naturally from this analysis as the Fourier conjugate of Δp_1 , the $\varphi_1-\varphi_2$ dimension. Specifically, transients for which $\varphi_1-\varphi_2=0$ cyc or $\frac{1}{2}$ cyc $(\pi$ rad) are the "CP" component and those for which $\varphi_1-\varphi_2=\frac{1}{4}$ cyc or $\frac{3}{4}$ cyc $(\frac{\pi}{2},\frac{3\pi}{2}$ rad) are the "CPMG" component.

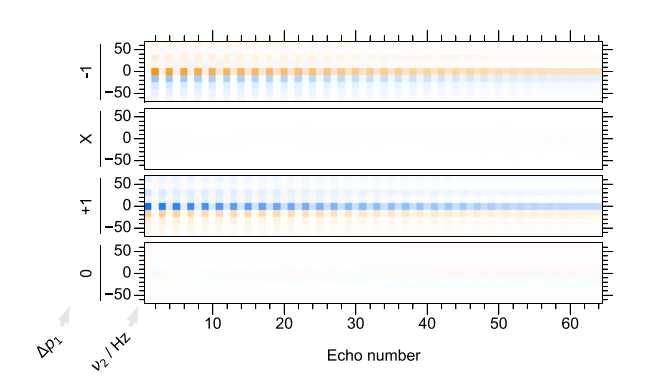


FIG. 9. CPMG data were acquired on high-field (400 MHz) Bruker spectrometer for 64 180° pulses. After each 180° pulse, the signal alternates between $\Delta p_1 = +1$ and $\Delta p_1 = -1$ until eventually bleeding is observed (by around the 12th echo).

In the case where field inhomogeneity is much smaller than the B_1 multiplied by the number of echoes $(\Delta \Omega \ll |\gamma B_1 n_{echo}|)$, both CP and CPMG signals present a significant amplitude.⁷⁹ The "bleeding" observed here illustrates the oscillation and decay of the CP component⁷⁹ arising from unanticipated storage of coherence along z [the red line in Fig. 8(b)] and clearly indicates when phase encoding information is not valid. Because only magnetization orthogonal to the direction of the pulse field in the rotating frame (e.g., x-magnetization subjected to a y pulse) is stored along the z axis, this affects only the CP transients of the phase cycle and not the CPMG transients. The resulting loss of phase-sensitive information, in turn, demands the application of an alternate acquisition scheme for many applications.⁷⁹ However, for various reasons, one may wish to harvest as much phase information as possible from the standard pulse sequence, while optimizing the SNR. Here, the DCCT map offers guidance on optimally filtering the signal. In the most rudimentary case, this involves zeroing the even/odd echoes of each pathway that contain only noise and frequency filtering along v_2 . This corresponds to preserving some information arising from the CP component.

The DCCT schema may also be applied to a CPMG measurement on a high-field spectrometer (Fig. 9). Here, the bleeding occurs at a later echo number due to the greater homogeneity of the superconducting magnet, pointing to the possibility of utilizing phase information as long as the number of echoes is kept limited.

Finally, note that these results represent examples where the phase cycling is constrained to a 90° step. Notable examples in the literature, such as the PIETA sequence, can maximize the use of concurrent phase cycles of multiple pulses for cases where finer-level phase incrementation is possible (and where DCCT coding and visualization should also prove fruitful).²⁸

D. Algorithms motivated and analyzed by DCCT

The remaining results introduce several realistic examples of how the DCCT map visualizes the transformation of the data from frequency domain untreated signal through phasing and alignment and ultimately through integration of the real part of the signal. Importantly, the DCCT schema provides a means for organizing and visualizing the data that enable the validation, implementation, and optimization of these algorithms for the purpose of analyzing

ODNP data. This section and Sec. IV D 3 are specifically attuned to acquiring ODNP data while Secs. IV D 1, IV D 2, IV D 4 and IV D 5 should prove of more general interest.

1. Phasing of echo-detected signal

In the field of quantitative NMR, various studies have treated the seemingly trivial, but ultimately pervasive and fundamentally linked, issues of automated baseline correction and first-order phase correction. ^{51,80,81} The presence of shot-to-shot instabilities of the magnetic field and the desire for a seamless transition between 1D spectroscopy and stroboscopic (e.g., CPMG) acquisition further complicates such attempts. As discussed in the theory section, i.e., Sec. II A 4, echo-based signals can simplify the timing/phase correction of the signal by removing the need to account for the distortion or loss of the first few points in the FID. Specifically, acquisition of echo-based signals replaces the potentially iterative phase and baseline correction with the problem of locating the center of the echo.

Figure 6(a) highlights the fact that even when the temporal (left to right) variation of the echo intensity is subtle, the phase (color) of successive echoes varies noticeably. This encourages the use of the full complex signal—i.e., phase as well as magnitude—from as much of the echo as possible in order to identify the echo center.

In fact, a simple algorithm that utilizes the phase information as well as the amplitude information of the echo can generate well-phased baseline-free signal from spin echoes. As a demonstration, a standard sample of water and TEMPOL generated a series of signals as part of a progressive enhancement sequence. Equation (10) calculates a cost whose minimum locates the center of an echo signal with Hermitian symmetry. Figure 10(a) displays this cost averaged across 28 indirect power steps at microwave powers ranging from 0 to 4 W. The cost function exhibits a well-defined minimum at $\Delta t_{\min}/2 = 10.6$ ms. After subtraction of this value from the time coordinates and application of a uniform zeroth-order phase correction to all scans, all signals display approximate Hermitian symmetry. The residual calculated by subtracting the signal from its Hermitian transpose $(s^*(-t))$ barely rises above the level of noise, and the imaginary components of all scans cross zero at t = 0 [Fig. 10(b)]. In other words, the detected echo accurately comprises a rising signal $(s_{rising}(t))$ for t < 0 and a mirror image (in the sense of Hermitian symmetry, such that $s(t) = s^*(-t)$) FID $(s_{FID}(t))$ for t > 0. Under standard electromagnet conditions, the refocusing of inhomogeneities is dramatic with $T_2^* \ll T_2$ and detection of echoes does not lead to a detectable decrease in signal amplitude relative to an FID acquired after a 90° pulse (Fig. SI-1). Finally, FID slicing [Eq. (3)] followed by Fourier transformation gives rise to in-phase, baseline-free signals [Fig. 10(c)].

Slightly longer echo times are preferred as they allow the spectrometer to acquire a sufficient amount of rising echo signal between the pulse dead time and the center of the echo. Echo times of as low as 3 ms enable Eq. (10) to easily determine the echo center for 15 MHz NMR. While the timing correction needed may be a conglomerate of various contributions, such as those mentioned in Sec. II A 4, the system in the authors' lab typically requires a timing correction of $100-500~\mu s$ relative to the expected center of the echo ($t_{echo} = \tau + 2t_{90}/\pi^{43}$). Repeated experiments typically reproduce the echo location satisfactorily and enable signal averaging.

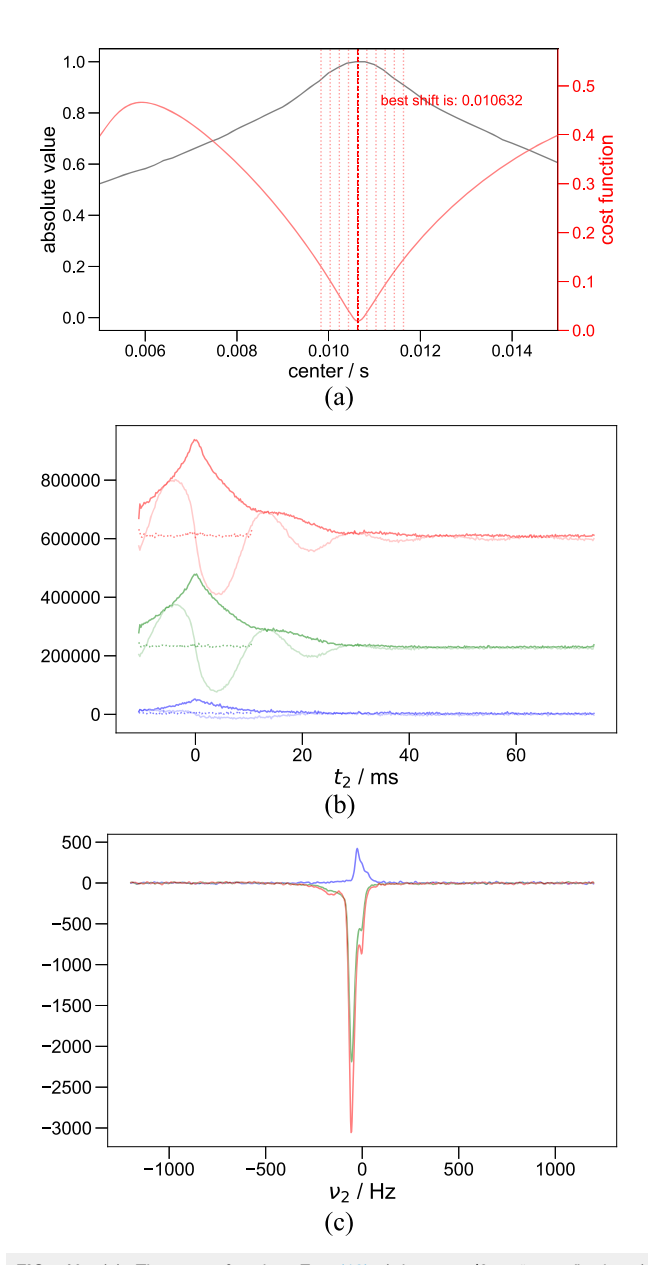


FIG. 10. (a) The cost function Eq. (10) (where $\Delta t/2$ = "center" above) demonstrates a clear minimum at the optimum time shift, $\Delta t_{\rm min}/2$, which represents the precise center of the spin echoes. Subtraction of $\Delta t_{\rm min}/2$ from the time axis centers the echoes at t=0. (b) After applying a uniform zeroth-order phase shift, the imaginary component of the echoes crosses zero at t=0 for all microwave powers employed to measure ODNP enhancement. Subsequent slicing of the FID from these echoes, following Eq. (3), yields well-phased, absorptive, baseline-free signal, the real component of which is shown in (c).

2. Simple NMR signal alignment

Even with a reasonable effort to maintain a stable resonance frequency, significant phase cycling noise tends to appear in the DCCT map of signal acquired on an electromagnet, as shown in and Fig. 12(c). Figure 11(a) illustrates the DCCT map of the signal from a simple spin echo with a short (\sim 1 ms) echo time on the 15 MHz electromagnet system, repeated for 10 scans (i.e., 10 complete phase cycles) for an aqueous 100 mM TEMPOL sample. During this relatively short echo time, the field has little opportunity to drift, and the signal refocuses at the echo center (t=0) almost completely and with a consistent phase. The amplitude of the phase cycling noise relative to the amplitude of the signal increases noticeably for times increasingly further away from the center of the echo. This effect matches the expected effect of a transient-to-transient variation of resonance (field) offset, which does not affect the signal at the echo center, but it does affect the evolution of signal phase moving away from the echo center. Thus, an initial inspection implies that a significant portion of phase cycling noise results from field fluctuations.

To ascertain the extent to which the presumed drifting of the static magnetic field is the cause of the phase cycling noise in Fig. 11(a), the iterative maximization of Eq. (23) (subjected to a Gaussian mask of width $\sigma=20$ and nonzero only for the coherence pathways $\Delta p_1=0$, $\Delta p_2=-1$ and $\Delta p_1=0$, $\Delta p_2=0$, as in) determines the frequency shifts required to align the individual transients, leading to the result shown in Fig. 11(b). The alignment mitigates the phase cycling noise while improving the consistency of the signal in the desired CT pathway. Thus, the signal alignment of Eq. (29) proves a viable means to address the experimental complications owed to randomly varying offset.

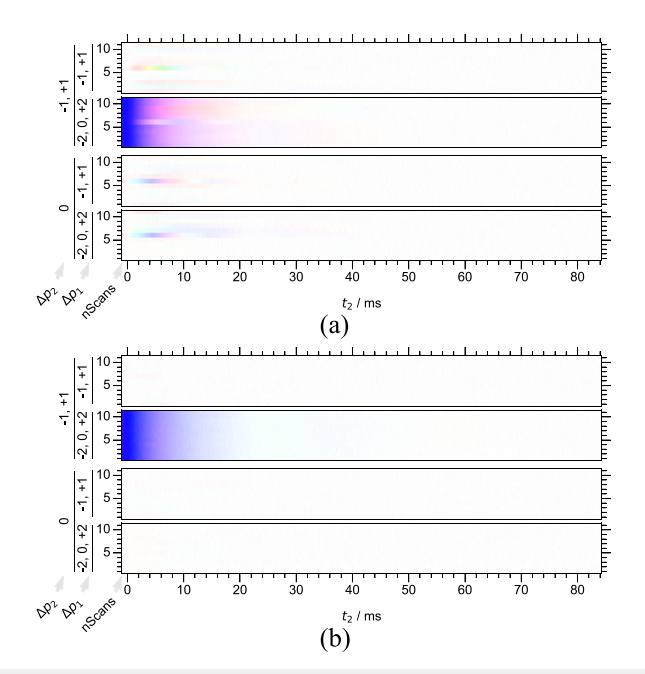


FIG. 11. The DCCT map (time domain) of a spin echo for 10 complete phase cycles with first-order phase correction. The undesired coherence pathways contain a significant amount of phase cycling noise [(a) note especially the 6th scan], which grows in amplitude moving away from t=0 before falling off as the signal dies off. The alignment procedure almost completely mitigates this phase cycling noise (b), as discussed in the text.

3. Example: Progressive enhancement

Figure 12 presents data for a progressive enhancement experiment for an aqueous 6 mM TEMPOL sample. Notable features of these data include an increase in signal intensity along the indirect dimension, p (μ w power), as well as an inversion of the data following the first indirect step (corresponding to the point at which ODNP polarization transfer exceeds the thermal polarization). First, Fig. 12(a) shows untreated data with two separate phase cycling (φ_1, φ_2) and direct (v_2) dimensions. This figure has been subjected only to a time domain Fourier transform and is included here as a conceptual aid: Note that viewing data in the phase domain rarely proves more diagnostic than viewing it in the coherence domain. A unitary Fourier transformation subsequently converts the phase cycling dimensions into the respective coherence domains, gathering the majority of the signal into the correct coherence pathway. This indicates that the majority of the equilibrium magnetization goes toward generating the signal of interest-as opposed to a situation where pulse misset or inhomogeneity expends a significant portion of the signal on artifactual pathways.

The Hermitian symmetry test enables an automated means to find and apply the timing correction [Figs. 12(b) and 12(c)]. Upon shifting t=0 to the center of the echo, much of the first-order phase error [which appears as a horizontal color variation in Fig. 12(b)] along the x-direction disappears [Fig. 12(c)], making the signal phase uniform across all frequencies and coherent (one color) along the indirect dimension. The correlation alignment [Figs. 12(c) and 12(d)] removes the scan-to-scan shifting of the signal and also relieves the slight phase cycling noise (a concept

introduced in Sec. IV C 3 and Fig. 7), as shown in Fig. 12(d). Finally, the data with integration bounds are shown in Fig. 14(a).

During the alignment procedure, five features prove to be essential. First, the algorithm must perform all timing (first-order phase) corrections before alignment since signals of different phases do not align properly. Second, a long acquisition (corresponding to a well-resolved, if noisy, frequency domain) capable of capturing sharp features yields the most dramatic improvements. Third, to allow for high resolution in the calculated $v_{shift, max}$, a significant zero-filling of the time domain together with a simple (exponential or Tukey) apodization precedes Fourier transformation to the frequency domain. Fourth, Eq. (23) requires a crosscorrelation function for each transient cross-correlated against all others, which permits higher SNR than, e.g., calculating only crosscorrelations for nearest-neighbor transients, as might be implied by Eq. (20). Finally, as noted in Sec. II A 6, optimizing the masked energy/norm of the signal, rather than the full energy/norm of the signal, proves to be essential. Once the echo signal is aligned, the FID is isolated [Eq. (3)] and its Fourier transform is shown in Fig. 14(a).

4. Line shape improvement and integration

ODNP and other low-field MR techniques require care when filtering and apodizing the data. Therefore, this section investigates the interplay of the DCCT technique with these methods.

To filter out unwanted frequencies in an experiment, the operator inspects the frequency domain DCCT map and slices out the portion of the frequency axis containing significant signal, thus

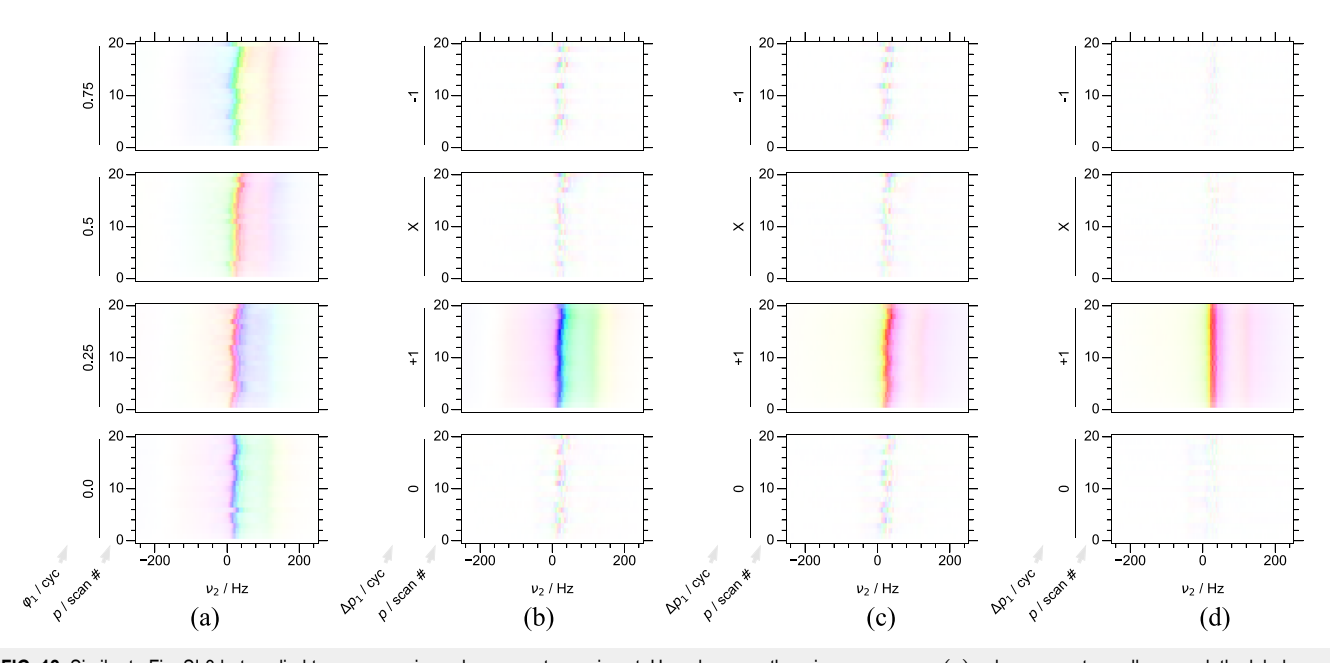


FIG. 12. Similar to Fig. SI-3 but applied to a progressive enhancement experiment. Here, because the microwave power (p) values are not equally spaced, the labels on the indirect dimension correspond to the scan number. (a) The untreated data are Fourier transformed only along the direct dimension. (b) Fourier transformation has been applied along the phase cycling dimension to yield coherence transfer dimension. (c) A timing correction corresponding to $\Delta t_{min}/2$ from Eq. (10) has been applied. (d) The data after applying the correlation alignment. Correlation alignment reduces the noise in the inactive channels by 60% (to $0.4 \times$ value before alignment), as a result of a reduction in-phase cycling noise. The 1D line plots for these data are shown in Fig. 14(a). In both (c) and (d), the FID has been sliced from the echo.

filtering out off-resonance noise and reducing the memory footprint of the signal. Domain coloring significantly assists in this process, since the incoherent noise appears as a multi-color scatter that can appear gray at a distance, while the weaker shoulders of peaks, etc., trend toward a common color, as exemplified in Fig. 15. The pySpecData library accepts slices given in frequency units (not requiring an array index) in a compact notation, as shown in listing A.6. It automatically recalculates the new time axis (since the slicing operation increases the spacing between the time domain datapoints).

Figure 13(a) presents preliminary data from an echo-detected inversion recovery experiment conducted on a sample of 150 μ M TEMPOL in toluene; this particular inversion recovery was conducted with no microwave power, thus without ODNP signal enhancement. For compactness, it shows only the coherence pathway of interest ($\Delta p_1 = +1$, $\Delta p_2 = -2$). This dataset presents a few challenges: SNR is limited, the acquisition time is relatively short—reflected here as a pixelation along the direct dimension

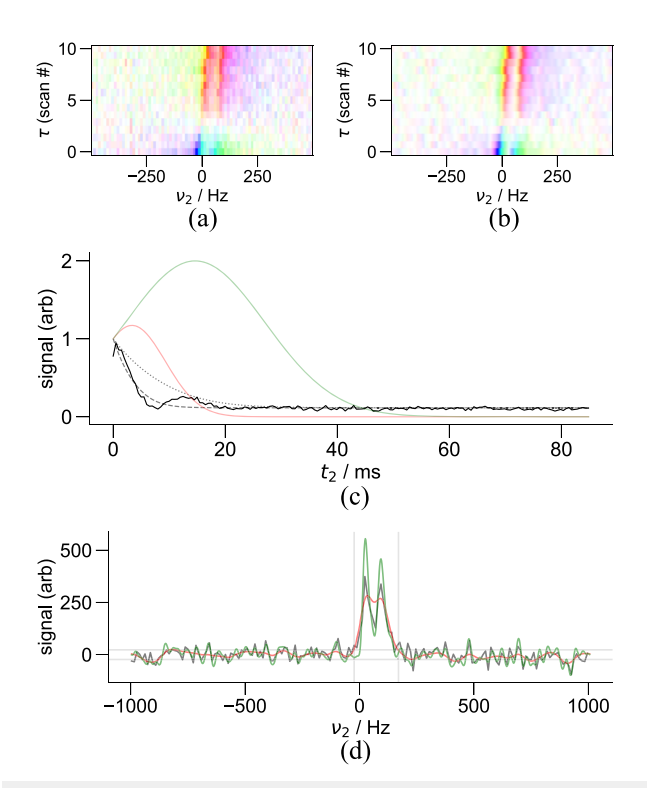


FIG. 13. NMR signal for an inversion recovery dataset of a 4.8 μ l toluene sample, showing the subset of the DCCT map (a) before and (b) after equal linewidth L2G apodization, which shows an improvement in resolution without a noticeable change in SNR. (c) The FID signal envelope (solid line) is fit to a model (dashed line) and then expanded to trace the envelope edge (dotted line), along with the resulting apodization functions with equal-energy L2G shown in red and equal linewidth L2G shown in green. (d) The real 1D spectra demonstrate the application of filters from (c), where red corresponds again to equal energy and green to equal linewidth, compared against the original 1D spectra in black. The gray horizontal lines superimposed on the spectra indicate the noise levels [from the fit in (c)] and the vertical lines suggest a choice of integration bounds.

(which has not been zero-filled)—and the resonance frequency varies slightly with the magnetic field of the electromagnet. Despite these issues, two distinct peaks (here vertical red bands of color) appear in the correct block of the DCCT map. Furthermore, despite the fact that the echo time is relatively short, Eq. (12) can determine the center of the echo to enable facile phasing. The peaks in Fig. 13(a) (blue-green at lower scan number and red at higher scan number) fade off into a constant yellow-green and purple color to either side of the direct frequency dimension. When properly phased, large portions of the dispersive tails of peaks present a constant imaginary phase that does not vary in phase with frequency (because the phase of a Lorentzian follows an arctan function as a function of frequency). Therefore, the yellow-green and purple regions are the dispersive tails of the resonance and the consistency of their coloration indicates that the FID has been correctly sliced from the echo with no further phasing correction required.

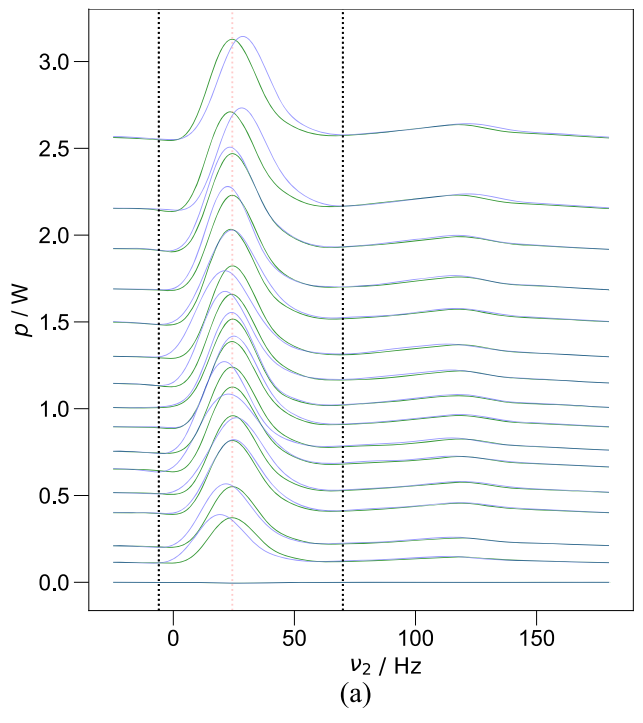
Most standard NMR data processing routines involve filtering in the time domain (apodization), with the specific goal of reducing or eliminating the contribution of noise from points where the signal has decayed to near zero and/or improving the spectral resolution. 82,83 However, this step requires more care than frequency domain filtering. Inhomogeneities frequently lead to sharp peaks in otherwise broad line shapes, meaning that signal in the direct time domain does not decay with a single T_2^* time constant. Optimal processing of ODNP data, therefore, requires acquisition with a long direct dimension (corresponding to more detailed frequency resolution) followed by apodization that filters out unnecessary noise. In particular, tests on the results acquired on customized instrumentation (where the acquisition length can sometimes be limited) indicate that proper treatment of the time domain signal is required for attempts at phasing by Eq. (12) or at alignment (as will be discussed later). Specifically, the acquisition length must either exceed $5/\pi \times$ the linewidth of the finest feature or else must be multiplied in the time domain by an exponential decay (i.e., apodized) whose time constant is at most 1/5th of the total acquisition length. For example, the proper application of Eq. (12) to generate Fig. 13(a) requires such apodization. While workarounds based on non-Fourier processing methods^{84–88} exist, attempts to ignore this reality using Fourier-based algorithms lead to issues with peaks either described by relatively few points (pixels in the DCCT representation) or subjected to dramatic sinc interpolation.

Ideally, knowledge of the time domain decay of the signal envelope guides the choice of a well-matched apodization function. The varying signal phase and frequency in Fig. 13(a) indicate a preference for finding the signal envelope by summing the absolute value of the individual scans in the time domain. A simple least squares fit of the result to Eqs. (15) and (17), in general, properly determines both the peak amplitude (A) and noise level (σ_n) of the signal. However, the least squares fitting algorithm adjusts the parameters associated with linewidth (λ_L) in a manner inconsistent with tracing the outer edge of the signal envelope—instead passing through the middle of oscillations. Therefore, keeping the same functional form, the code scans from a minimum λ_L (here, typically 10 Hz) up to the least squares fit value of λ_L , and it determines the norm of the data exceeding the fit function at each linewidth. The point where this norm is a fifth of the way from its lowest value to its highest value (at

the least squares λ_L) is chosen as the λ_L of the envelope. The dotted line in Fig. 13(c) shows the envelope calculated for the toluene data.

Armed with this choice of an enveloped-matched filter [Fig. 13(c)], the results of Fig. 13 explore the impact of some common apodization functions. Some instances of ODNP benefit from the ability to resolve chemical shifts as demonstrated recently in several contexts. 19,58,89 In Fig. 13(b), an equal linewidth L2G transformation [Eq. (19)] aids the resolution of two peaks in the NMR spectrum without noticeably degrading the SNR. Notably, the apodization emphasizes a faint white region between the peaks with neither dispersive/imaginary (yellow-green or purple) nor absorptive/real (red) signal. Figure 13(d) demonstrates the same effect in 1D format and also the impact of an equal-energy L2G transformation [Eq. (18)], which slightly degrades resolution but significantly reduces the noise. It is also interesting to note that (not shown here), by emphasizing particular regions of time, the apodization function can have a notable effect on the inactive pathways in the coherence domain, reducing some phase cycling noise and/or reducing the amplitude of artifacts that occupy different portions of the time domain vs the signal. The equal-energy transformation improves the SNR of the peak, without significantly broadening the range over which it is nonzero. A procedure to automate the choice of integration bounds can apply Eq. (18) and also use the σ_n fit from the envelope equation [Eq. (17) and Fig. 13(c)] to determine the integration bounds from the points where the (equal-energy L2G) apodized peak intersects with 0.5 the standard deviation of the noise of the original spectrum. The gray lines in Fig. 13(d) provide an example of the procedure for the present data. Overall, the results shown and discussed here emphasize that standard L2G apodization techniques provide significant benefit to processing low-field ODNP data, and that the DCCT map provides a facile means to assess this signal improvement. As noted in the theory section (Sec. II A 5), L2G apodization allows for many choices of relative Gaussian and Lorentzian linewidths; the results here show that the choice designated as "equal energy" improves the SNR of the data significantly, while the choice designated as "equal linewidth" improves the resolution without appreciably degrading the signal-to-noise ratio. Every rigorous ODNP dynamics analysis following the current standard protocol¹¹ demands a means to easily process the untreated data and unambiguously determine the relevant parameters (see Sec. II B) without significant user input. An important component of this challenge involves converting spectra along the direct dimension (v_2) into signal intensities. Figure 14 compares data that was not aligned (blue) to data that was aligned (green), according to the alignment routine described in Sec. II A 6, prior to integration. The blue spectra and integrated datapoints correspond to Figure 12(c) and the green correspond to Figure 12(d).

After slicing out the FID from the data of Fig. 12(d), the code applies an equal-energy L2G apodization [Eq. (18)] to improve the SNR of the signal. Because these data come largely from highly enhanced signal, the result gives a controlled example where the main concerns focus on issues of field stability and misalignment. The stability of the signal is somewhat run-dependent, with the data in Fig. 14(a) an example of fairly stable progressive enhancement signal. While the line shape of the aligned signal (green) remains relatively consistent, the line shape of the unaligned signal (blue) slightly varies—not only in the position of the central peak but also in terms of subtle variations of the shoulder. While



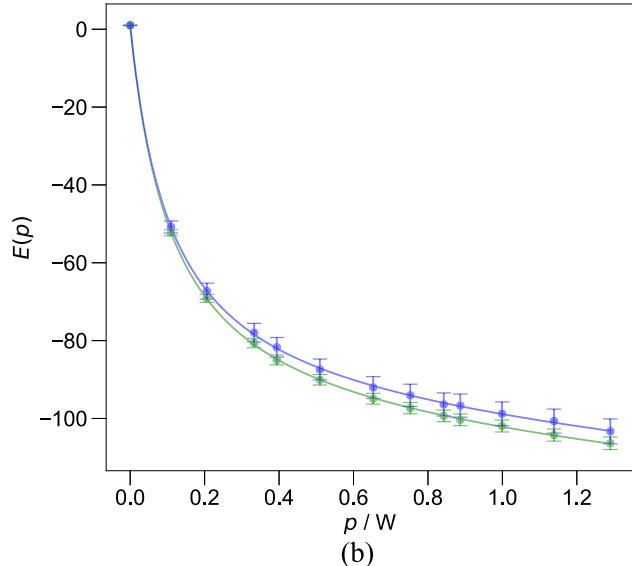


FIG. 14. The NMR signal intensity is determined for a progressive enhancement experiment on 6 mM aqueous TEMPOL (same data as Fig. 12), both without (blue) and with (green) alignment. (a) The real part of the spectrum after slicing out the FID and applying equal-energy L2G apodization with integration limits indicated, before alignment in blue and after alignment in green. The dashed vertical lines provide the integration bounds, while the red line provides a guide to the eye. All signals have been inverted and two scans have been omitted for the sake of presentation clarity. (b) Normalized integral intensities are denoted by circles with accompanying error bars, while the smooth line gives the least squares fit to Eq. (30). Both sets of data were phase corrected. In both cases, error propagation of the noise in inactive coherence channels gives the noise of the integrals, which standard error propagation formulas then modify upon normalization. Correlation alignment refines integration bounds, overall improving the SNR.

the unaligned signal demands integration over fixed bounds, the aligned signal proves amenable to a weighted sum over the line shape, resulting in tighter error bars (propagated from the noise of the datapoints) that produce a tight match to the model (R^2 0.9987 for unaligned 0.9995 for aligned). The overall scaling of the error bars for the unaligned integration proves very sensitive to the choice of integration bounds (data not shown); however, no such ambiguity exists for the weighted average. This offers promise for not only the precise quantification of important reference standards for ODNP, as done here, but also for a complete ODNP analysis of samples with very low concentrations of either spin label or water.

5. Example: Thermal scan on reverse micelles

Typical ODNP studies rely on the fact that water comprises most of the sample, enabling the use of relatively small sample volumes (\sim 4.8 μ l). Studying the water inside reverse micelles proves challenging, as the proton spectra present \sim 1/30× the SNR of aqueous samples. However, with longitudinal relaxation rates, R_1 , that are significantly faster (e.g. \sim 7.7 s $^{-1}$) than those of aqueous solutions (\sim 0.4 s $^{-1}$), reverse micelles provide an opportunity for rapid signal averaging not otherwise possible in typical ODNP samples. ODNP studies of solutions of organic solvents typically employ larger sample volumes (even in recent studies 90), following the rationale that much of the sample is made of low-loss dielectric

solvent that can extend into the electric field of the cavity with less substantially detrimental heating effects. However, water and dielectrically active surfactant comprise an uncomfortable intermediate fraction of the sample, resulting in a lower water NMR signal density but still (based on changes to cavity Q) presenting a significant concern with respect to sample heating. Thus, even though initial reverse micelle studies used large probes and subsequently larger sample volumes, 17 studies of the dynamics of water inside the reverse micelles still require a small (\leq 0.6 mm) sample radius in order to minimize heating effects.

Figure 15 shows a portion of the DCCT map for thermally polarized spin echo NMR signal for a reverse micelle sample. To compensate for the very low ¹H content of this system, the pulse sequence cycles through the 8-step spin echo phase cycle 200 times, resulting in 1600 individual transients. The 1D plots at the top of Fig. 15 show the spectrum from one complete phase cycle (i.e., one scan) in blue as well as the average over all 200 scans in red. While individual transients have insufficient SNR to clearly identify the signal, acquiring many transients can lead to broadening of the averaged signal in the presence of slow field drift, rendering the characterization of thermal signals particularly problematic. In contrast to either of the 1D plots, the DCCT map shows an obvious red band of signal in the expected coherence channel at +75 Hz offset. It also shows that the signal appears to randomly drift over 50–75 Hz throughout the course of the experiment.

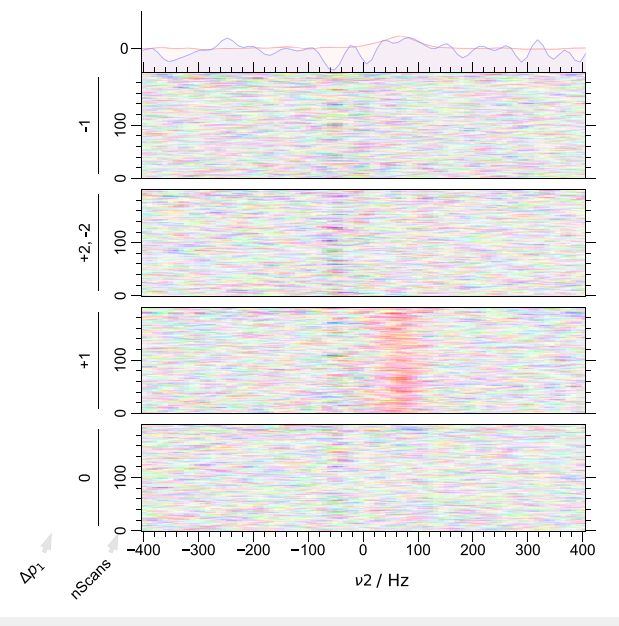


FIG. 15. A portion of the DCCT map for the signal from a reverse micelle sample, before undergoing the correlation alignment. The DCCT map allows the separate display of scans while also emphasizing the phase-coherent signal. This map only shows the $\Delta \rho_2 = -2$ portion of the coherence domain for the second pulse as the other CT pathways include only noise similar to the noise-only pathways that are shown here. The signal appears in red in the expected pathway but is very faint. The 1D plots illustrate that the signal is not observable from a single phase cycled scan of the 1600 scans (blue) and is faintly detectable upon averaging over all of the scans (red).

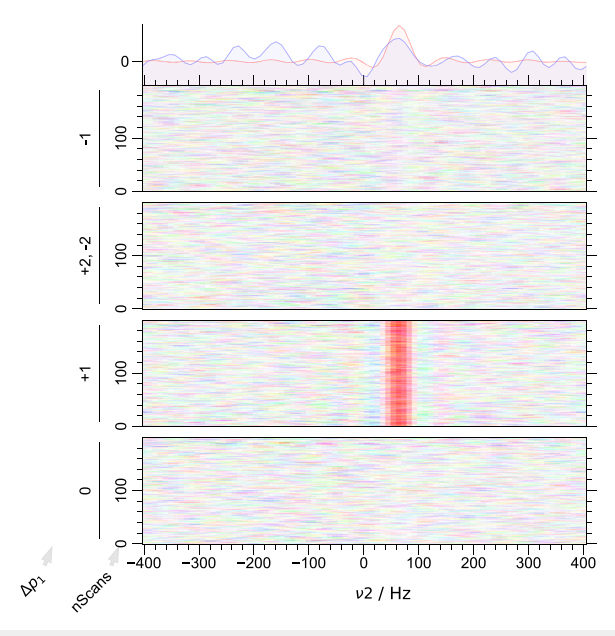


FIG. 16. The same portion of the DCCT map for the data in 15 after undergoing the correlation alignment in Eq. (29). The signal concentrates into a bright red band in the appropriate coherence pathway. The 1D plots illustrate that the signal is marginally observable from a single scan out of the 1600 scans (blue); this arises from the alignment of the various transients in the phase cycle. An average taken over all scans significantly improves the signal amplitude (red) and does so with much greater efficiency when the signal has been previously aligned than in the absence of alignment.

Despite the low SNR of the experiment, the signal-averaged correlation function [Eq. (23)] should still be able to align the various transients, since each of the correlation functions used to determine the frequency shifts is averaged from 200 separate correlation functions (one for each pair of transients in the experiment). Indeed, after the correlation alignment (Fig. 16), the signal again appears in the expected coherence channel, but now as an even more distinct band of a solid color that spans the 200 phase cycled transients-namely, the intense red band at 50 Hz, with blue side bands arising from truncation of the rising portion of the echo. The 1D plot shows that, after the correlation alignment, the signal is observed after a single phase cycle (blue), and it is improved and reduced in noise significantly after averaging over all 200 cycles through the phase cycle (red). This signal exhibits a significantly reduced linewidth of ~125 Hz, explained by the alignment of the consecutive transients shown in Fig. 17.

Even though the net signal energy, averaged across repeats, remains the same, aligning the signal improves the phase coherence of the signal from transient to transient. Figures 15 vs 16 demonstrate a visual explanation of this process that improves the SNR slightly within each phase cycled scan. A visual effect arising from the improved phase coherence between adjacent scans also likely contributes to the increased visibility of the signal in Fig. 16. Overall, the signal-averaged alignment makes the signal much more

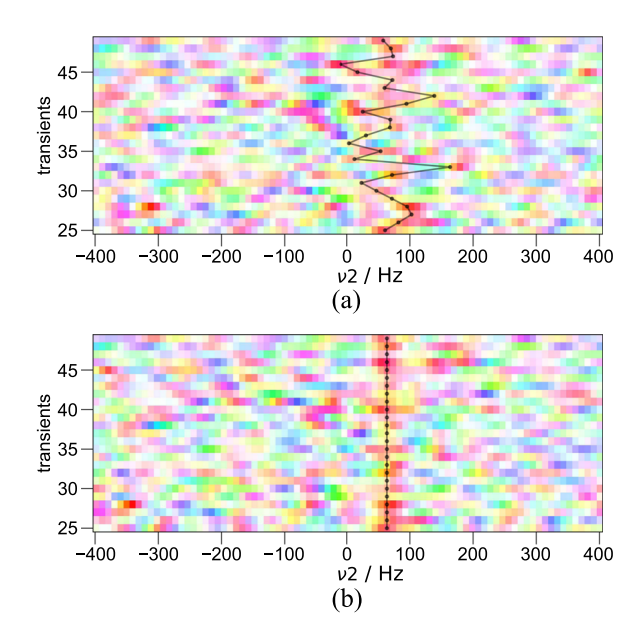


FIG. 17. (a) The DCCT map shows only 50 transients of the coherence channel of interest, for the reverse micelle sample in Sec. IV D 5 before undergoing the correlation alignment. The transients axis represents a direct product of the pulse phase dimensions and the nScans dimension of Figs. 15 and 16. A black line at 50 Hz indicates the expected signal offset. (b) After undergoing the correlation alignment, the signal is clearly discernible from noise as a red streak across all scans centered at 50 Hz (indicated by the black line). Note that the alignment routine chooses the center of the signal to be not only typically in-phase red (0°) signal but also that the signal ∼ 40 Hz to the left (smaller frequencies) of the chosen point is more frequently purple or blue (−60° or −120°) when compared to frequency with random noise.

visible not only in the averaged signal but also within the individual scans displayed in the DCCT map. This is a striking and somewhat unexpected result.

V. DISCUSSION

The results here advocate for a nonstandard approach to utilizing coherence pathways. The DCCT schema comprises four interdependent features: (1) storage of all transients (i.e., not phase cycling the receiver and/or averaging on board), (2) multidimensional organization of data, (3) object-oriented code that assists in data manipulation, and (4) visualization of data as a DCCT map at a relatively early stage of data processing. To summarize and contextualize the various results presented here, Fig. 18 provides a flowchart visualization of the DCCT schema.

The visualization of all separable coherence pathways along an additional, short dimension enables efficient diagnosis and mitigation of effects as simple as instrument miscalibration and as subtle as the phase cycling noise caused by unstable fields. In fact, as shown in Sec. IV C 1, less specialized equipment—i.e., hardware without the capability to phase cycle the receiver—require this approach in order to separate the desired signal from undesired artifacts.

One notable observation is the fact that domain coloring combines synergistically with the simultaneous presentation of multiple CT pathways. In particular, domain coloring enables the straightforward, simultaneous visualization of all CT pathways by bypassing complexities that arise when different pathways have different phases or timings and/or varying resonance frequencies. By offering a direct, compact visualization of phase coherence as pixels of matching or slowly varying color, the DCCT map also serves as an excellent tool for detecting signals that might otherwise appear to be only noise. In contrast, a lack of coherence, e.g., between echo centers of subsequent scans in the presence of field instabilities (Fig. 6), also becomes quite obvious. Observation of low SNR DCCT maps motivated the development and implementation of the signalaveraged mean-field correlation alignment presented here, which results in a very clear improvement in the signal linewidth, SNR, and the means for quantifying signal.

While traditional techniques involve discarding at least some data (undesired CT pathways, the imaginary part of data, etc.), DCCT maps afford a comprehensive overview of all acquired data in one image, at a very early stage of data processing. Importantly, the DCCT map can yield these results and other informative comparisons between datasets without first requiring detailed phasing or other manipulation of the untreated datasets (Figs. 2, 3, and 5). Thus, the DCCT schema enables deterministic and rapid progress toward acquisition and optimization of NMR signal. The studies here, in particular, demonstrate that DCCT maps prove invaluable in the initial stages of instrument setup, as well as in diagnostic efforts for failed experiments—e.g., the incorporation of new probes or receiver chain components—thus providing significant support for instruments with modular capability. These results also showcase the ability of the DCCT map to highlight three important features of the data: (1) the desired signal in the desired CT pathway, (2) artifacts arising from artifactual pathways and potentially contaminating the desired pathway, and (3) phase cycling noise spread across multiple pathways.

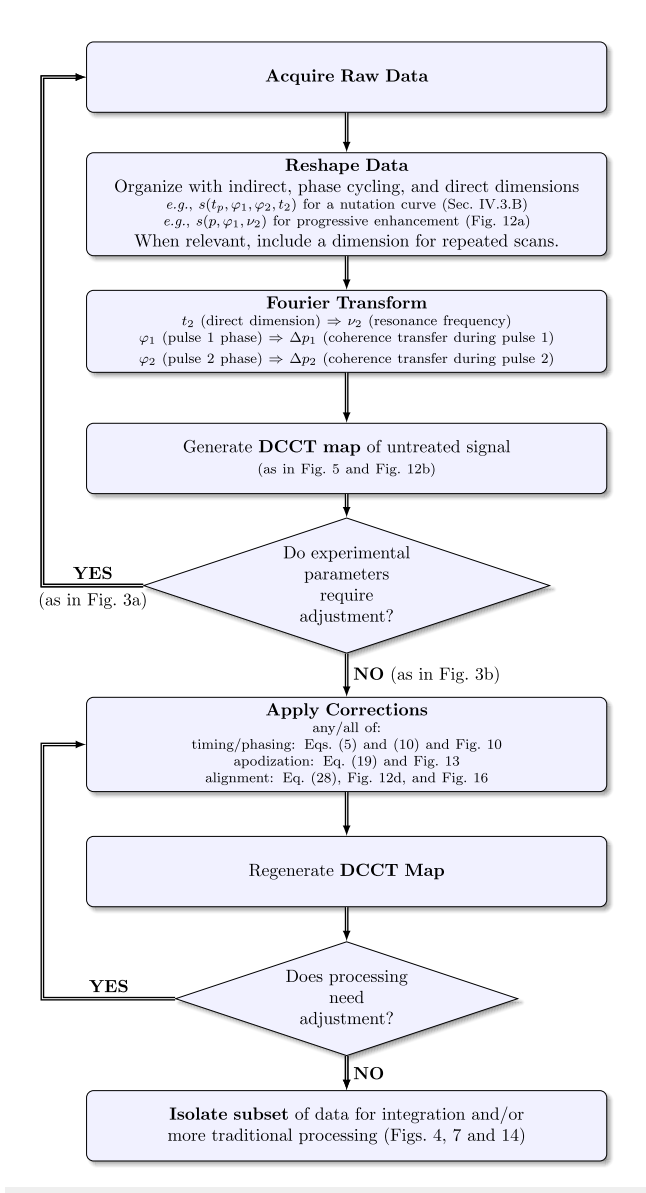


FIG. 18. A flowchart depicting the DCCT schema. A selection of references to figures and text sections are provided as examples. Here, the term "indirect" dimension refers to a dimension along which an experimental parameter delay length, microwave power, or pulse length changes, "direct" dimension refers to the dimension along the length of digitization (i.e., successive points of an echo or FID acquisition), and "scans" refers to exact repetitions of a phase cycled pulse sequence (repeated to improve SNR).

An argument can be made that standard data processing technology frequently lags behind the established understanding of coherence pathways by jumping straight to the selection of the desired coherence pathway. Even though researchers are aware that detailed analysis of coherence pathways could enrich experimental design, 91 and one could infer similar gains by extending such an analysis to the development of data processing algorithms, it has been frequently necessary to skip the development of such

algorithms due to the resulting complexity and incompatibility with standard acquisition techniques and data processing software. As has repeatedly been noted in the literature, ^{26-28,30,31} the days before direct detection and digital filtration of rf signals (when limited memory space requirements and slow data transfer rates were a primary concern) have left many historical artifacts that continue to impact typical current approaches to NMR data acquisition and processing. In particular, the rather stringent constraints of minimizing the size of temporarily stored time domain data through onboard averaging of transients acquired with different phases motivated the design of what has become the traditional methodology for treating coherence pathways in NMR.⁷⁴ While the traditional schema still proves optimal in many cases, equipment available today welcomes virtually cost-free storage of all transients in a phase cycle. The DCCT schema outlines a straightforward means to profit from these benefits via object-oriented treatment of the resulting multidimensional data and robust multi-color domain coloring plots. Importantly, it does not add any time cost to a more traditionally acquired NMR

The DCCT approach is not without historical precedent. Very early examples within the context of multiple quantum spectroscopy^{25,29,69} explicitly Fourier transform along a dimension where phases were cycled in a procedure formalized as the "Phase Fourier transform." More recently, separate storage of the transients to perform this transformation has proven advantageous in 2D multi-quantum experiments, such as in multiplex phase cycling²⁶ and MQD²⁷ as well as in echo train experiments.²⁸ It is therefore important to note that many modern laboratories utilize a methodology similar to a subset of the DCCT schema, although the authors are unaware of an extant formal description of this very useful procedure in the literature, nor of a consistent and convenient accompanying data visualization technique, like the one presented here. As observed in the current contribution, the general concept garners the widest utility when also used as a means to explicitly consider signals in regions of the coherence domain that are not selected by the pulse sequence.

The DCCT schema, further, offers a means for visually representing several known but important properties of phase cycling. For example, Plancherel's theorem emphasizes that the noise from different transients in the phase cycle domain will spread equally across the coherence domain. Therefore, the selection of a single coherence pathway yields the same SNR benefit as (not phase cycled) signal averaging. The low-field experiments in the results here typically benefit from the added SNR of additional phase cycling, since these studies tend to be SNR-limited. However, for the implementation of more elaborate pulse sequences, one desires a straightforward strategy for choosing an optimal phase cycle. 91 The DCCT schema offers such a strategy. Specifically, a DCCT map of signal from a comprehensive phase cycle (e.g., where all pulses are phase cycled by four or more steps) would clearly show where in the coherence domain (for which values of Δp_1 , Δp_2 , etc.) artifacts occur and where they do not occur; this clearly indicates which parts of the phase cycle can be reduced and which cannot. Eliminating or reducing the number of phase cycle steps for pulses whose coherence domain shows only noise along one or more dimensions only decreases the SNR. In contrast, eliminating or reducing the phase cycle for pulses where the coherence domain shows artifactual

signal will alias those artifacts,²⁵ potentially into the desired coherence pathway.

As a simple example, in Fig. 5, elimination of the phase cycle of the first pulse would add the noise of the $\Delta p_1 = \pm 1$, $\Delta p_2 = \pm 1$ pathway to that of the $\Delta p_1 = 0$, $\Delta p_2 = -1$ pathway and the noise of the $\Delta p_1 = 0$, $\Delta p_2 = 0$ pathway to the $\Delta p_1 = +1$, $\Delta p_2 = -2$ pathway. While this decreases the SNR by $\sqrt{2}$, the artifact ($\Delta p_1 = 0$, $\Delta p_2 = -1$) remains separated (no significant DC artifacts at $\Delta p_1 = 0$, $\Delta p_2 = 0$ are present here) and the number of scans reduces by a factor of 2. In contrast, elimination of the phase cycle altogether adds all four coherence pathways together, superimposing the FID-like artifact in $\Delta p_1 = 0$, $\Delta p_2 = -1$ onto the actual echo signal in $\Delta p_1 = +1$, $\Delta p_2 = -2$. Similarly, the CPMG results in Fig. 8(a) indicate when a four-step vs two-step phase cycle of the excitation pulse proves useful. These are simple examples, but they provide a demonstration of an empirical method that can be extended to more complex pulse sequences.

For application to experiments in electromagnets and other nonideal fields, the results here advocate a strategy of acquisition lengths spanning many times the T_2^* (with ideal timescales governed rather by the sharpest features of the line shape), with phasing identified from the Hermitian symmetry of the echo signal (Sec. II A 4), followed by alignment (Sec. II A 6) and apodization (Sec. II A 5). The benefits of echo-based detection complement the DCCT schema, as echo-based signal follows a distinctive coherence pathway. Thus, phase cycled echoes offer particular advantages over 90° pulse-acquired schemes when acquiring signal on a system for the first time. Aside from offering a maximum signal intensity that is not sensitive to field inhomogeneity, echo signals are also cleanly isolated from any ringdown arising from the pulses. The signal appears in one out of the eight separate pathways in the coherence domain that are resolved by a typical phase cycle, and it can be compared to the amplitude of the noise and artifacts of signal in these other pathways. Furthermore, echo-based signals do not require post-processing (e.g., linear prediction or polynomial fitting) to yield baseline-free spectra, which here proves ideal for the quantitative NMR necessary for

Similarly, standard apodization techniques, such as L2G, prove useful for resolving and quantifying the signal intensity of these low-field data acquired in unstable magnetic fields. It stands to reason that, though beyond the scope of this publication, extension to reference deconvolution would likely further improve the quality of these results. 92

Beyond these specifics, however, the most important result reported here is the unexpected synergy between domain coloring for the visualization of signal phase, the simultaneous visualization of all coherence pathways, and modern object-oriented programming that enables organization and plotting of the data.

VI. CONCLUSION

The DCCT schema offers a powerful new standard for visualizing data (the DCCT map) that proves unexpectedly useful and versatile. The results presented here highlight the DCCT schema as critical for quickly identifying and optimizing signal in the presence of obstacles such as inhomogeneous fields or reduced

SNR, as in low-field NMR. As repeatedly noted in the literature, eschewing onboard signal averaging offers a range of practical benefits, but beyond this, the DCCT schema provides a detailed yet comprehensible view of all of the data acquired during the course of an NMR experiment, leading to a significant degree of confidence in the quality of the results and subsequent data processing.

This technique also serves as a means to elucidate experimental errors that otherwise would be overlooked, serving to improve the overall execution of NMR. Furthermore, the use of the DCCT map to visualize the complete suite of coherence transfer pathways attainable for a given pulse sequence offers insight into empirical phase cycle optimization for a given experiment. The success of these methods in improving the practicability of the modular ODNP system here indicates future successes in other fields of customized NMR. Due to these benefits, the DCCT map will serve as an excellent tool for detecting signal whether in routine spectroscopy of biomolecules, in a spectrometer subjected to appreciable field drift, or in samples with challenging low proton concentrations that would otherwise produce only noise. The ability of the DCCT map to aid in detecting signals despite significant noise has applications to low-field systems as well as when dealing with simple but costly human errors on well-configured high-field

Finally, the DCCT map is expected to contribute to aid in the development of data processing routines and algorithms, such as the signal-averaged mean-field correlation alignment presented here, given its ability to highlight shortcomings in the execution of NMR experiments. The authors foresee benefit from the DCCT plotting methodology in areas of low-field NMR, such as portable NMR,⁵⁰ high resolution ODNP, 19 and 2D Overhauser ODNP, 58 as well as areas of high-field NMR where signal alignment is of concern.⁵³ Furthermore, this technique could apply well to intermolecular multiple quantum coherence experiments⁹³ and pulsed ESR.^{94,95} In ESR spectroscopy, separate storage of all transients can prove prohibitive, but separate storage of different steps of the phase cycle (averaged across repeated scans) should prove feasible, especially on custom systems.⁹⁶ However, the target of future applications ranges broadly, from experiments as closely related as portable MR to those as distantly related as two-dimensional coherent laser spectroscopy.

SUPPLEMENTARY MATERIAL

See the supplementary material for further details regarding data handling and an additional application of the processing techniques.

ACKNOWLEDGMENTS

This work was supported, in part, by the National Science Foundation under Grant No. 2146270. This work was also supported, in part, by the Syracuse University College of Arts + Sciences in the form of startup funds and the Graduate School Summer Dissertation Fellowship received by AAB. The authors would like to thank all the members of ACERT and Professor Jack Freed's lab as well as members of Professor Songi Han's lab for

fruitful discussions and the opportunity to develop nascent stages of the concepts presented here. The authors would also like to thank the ODNP team at Bridge12 and Dr. Tom Casey for fruitful discussions and to note that several features of the pySpecData library have also been ported to the DNPLab Python package available at http://dnplab.net/ for broader dissemination to the community.

AUTHOR DECLARATIONS

Conflict of Interest

The authors have no conflicts to disclose.

Author Contributions

Alec A. Beaton: Conceptualization (supporting); Data curation (equal); Formal analysis (supporting); Investigation (lead); Methodology (lead); Software (equal); Validation (equal); Visualization (equal); Writing – original draft (lead); Writing – review & editing (equal). Alexandria Guinness: Data curation (equal); Investigation (supporting); Methodology (equal); Software (supporting); Validation (supporting); Visualization (equal); Writing – review & editing (supporting); Formal analysis (lead); Funding acquisition (lead); Investigation (supporting); Methodology (supporting); Project administration (lead); Resources (lead); Software (lead); Supervision (lead); Validation (supporting); Visualization (equal); Writing – review & editing (equal).

DATA AVAILABILITY

Untreated datasets underlying all figures are stored in HDF5 format and are freely available from the authors upon request.

APPENDIX: CODE SNIPPETS

The FID is sliced from the echo by subtracting the delay between the start of acquisition and the center of the echo, t_{delay} from the original t_2 axis coordinates, then placing the axis in register (so that one of the axis coordinates occurs at exactly $t_2 = 0$), slicing out only values $t_2 > 0$, and finally setting the first datapoint to 1/2 its original value.

Listing A.1. FID slice

Pulse programs supplied from Bruker implement the "traditional" schema for phase cycling, that is, cycling of the receiver

phase and signal averaging on board. In order to store all the phase cycled transients separately, slight modifications to existing pulse programs are needed. The following demonstrates a template that has been successfully used to accomplish this task in a Bruker pulse program:

Listing A.2. Separately saved phase cycling in Bruker pulse program

```
"121=4" ; length of phase program ph1
"122=2" ; length of phase program ph2
   loopcounter num_ph
   "num_ph = 121*122"
   ; td1 set to total number of transients
     (including the phase cycle)
   "120 = td1/num_ph" ; calculates indirect
                        ; dimension, if it exists
   "nbl = num_ph"
10
          st0 ; reset buffer pointer to 0 when
              ; phase cycle is complete
12
         p1 ph1; apply 90 pulse according
13
                  ; to phase program ph1
          ; (rudimentary template showing only key
15
          ; features -- delays, etc are omitted.
16
          ; A standard spin echo would have a
          ; delay here.)
18
         p2 ph2; apply 180 pulse according
19
                ; to phase program ph2
          goscnp ph31 ; acquisition of data,
21
22
                       ;rx phase always 0
23
          ipp1 ; increment phase of first pulse
24
          lo to 2 times 121 ; controls loop over
25
26
                             ; phase program ph1.
27
                             ; By convention, we
28
                             ; use loop counter
                             ; 12% for phase
29
30
                              ; cycle X
         ipp2 ; increment phase pointer
31
32
               ; to program ph2, as outermost
               ; phase cycling loop
33
       lo to 2 times 122
34
     \boldsymbol{wr} #0 if #0 id0 ; even for experiments that
35
     ; don't require d0, id0 is required for
     ; standard behavior
37
   lo to 1 times 120 ; if indirect dimension
38
                       ; employed, this loop
                       ; generates the indirect
                       ; dimension
41
   ; phase programs
43
   ph1 = 0 \ 1 \ 2 \ 3
44
   ph2 = 0 2
   ph31=0 ; receiver phase, always 0
   ; note through loops and phase pointers,
47
   ; we avoid:
   ; ph1 = 0 1 2 3 0 1 2 3
   ; ph2 = 0 0 0 0 2 2 2 2
```

The following pySpecData Python library easily sets the time axis of the data to center the echo at t=0. The data instance "s" is either directly supplied by the spectrometer (utilizing an in-house library for running the SpinCore transceiver) or by loading the

relevant Bruker data into pySpecData. Here, we assume that "s" was previously moved from the direct time to frequency domain (e.g., in order to slice out a relevant range of spectral frequencies).

Listing A.3. Setting time axis

Acquisition with the digital oscilloscope requires digital demodulation and filtering, which typically takes the following form. (Note how the time domain name for the axis is typically used to refer to the axis, regardless of whether it is currently in the time or frequency domain.)

Listing A.4. Oscilloscope-based acquisition

```
with GDS_scope() as g:
       pulse = g.acquire_waveform(
2
           ch=1
          # typically, split off and capture the
           pulse waveform for reference
5
       s = g.acquire_waveform(
           ch=2
         # signal after duplexer and LNA
       pulse.ft(
           "t", shift=True
10
          \# move the pulse waveform into the
11
          frequency domain
12
       center_frq = abs(
13
               pulse["t":(0, None)]
14
               ).argmax("t") # estimate the
15
                                 carrier frequency
16
                                 from the max
17
18
       s.ft(
           "t", shift=True
         # move the signal into the time domain
20
21
       s = s \lceil
           "t" : (center_frq + r_[-10e3, 10e3])
         # filter out a 20 kHz bandwidth
23
       s.ift("t") # move s back to the time
24
                      domain
```

Storing each phase cycled transient separately results, in the simplest case scenario, in one long concatenated sequence of complex data (one-dimensional array). One can easily reshape this long one-dimensional array into the appropriate dimensions of choice, an operating referred to in pySpecData as "chunk"-ing.

Listing A.5. Example of chunking data for DCCTF

```
s.chunk(
2
        "t", ["ph2", "ph1", "t2"], [2, 4, -1]
       # here we break data into phase cycle
3
         \texttt{steps} \rightarrow \texttt{assuming} \ \texttt{that} \ \texttt{the} \ \texttt{leftmost}
   #
         dimension is iterated by the outermost
         loop of the pulse sequence while the
6
   #
         rightmost label is iterated by the
7
   #
         innermost loop of the pulse sequence
8
         (typically the counter for the direct
9
        acquisition datapoints)
10
   s.setaxis(
11
12
        "ph1", r_[0:4] / 4
        label the phase cycling dimension, in
13
        units of cycles -- the first pulse here
14
   #
15
         is cycled in 4 steps
   s.setaxis(
16
        "ph2", r_[0:2] / 4
17
18
       \# label the phase cycling dimension, in
        units of cycles -- the second pulse here
19
   #
         is cycled in 2 steps
20
21
   s.ft(
        ["ph1", "ph2"], unitary=True
22
   )
      # Fourier Transform to move from the phase
23
24
         cycling domain to the coherence domain 
ightarrow
         this example employs a vector-unitary
25
   #
         Fourier Transformation (which preserves
26
   #
27
        the vector norm)
28
        "t2", shift=True
29
       # Fourier Transformation from the time to
30
        frequency domain along the direct
31
         dimension
32
33
   DCCT (
        s["t2":(-500, 500)]
      # generate a DCCT plot over the
35
36
        range \pm 500 Hz
```

The following demonstrates the ease with which one can filter along a given axis (here, frequency filtering) in pySpecData, referring to values along the axis itself, and returning data along that slice.

Listing A.6. Frequency slicing

```
s.ft("t2", shift=True) # Fourier Transform
                             (shifted to center
2
                             about 0 Hz) from the
3
  #
  #
                             time to frequency
4
5
  #
                             domain along the
                             direct dimension.
6
  s = s["t2":(-400, 400)] # slice out the signal
7
                              within \pm 400 Hz of
9
                              the carrier
```

REFERENCES

¹B. D. Armstrong and S. Han, "Overhauser dynamic nuclear polarization to study local water dynamics," J. Am. Chem. Soc. **131**(13), 4641–4647 (2009).

²J. M. Franck, A. Pavlova, J. A. Scott, and S. Han, "Quantitative cw Overhauser effect dynamic nuclear polarization for the analysis of local water dynamics," Prog. Nucl. Magn. Reson. Spectrosc. 74, 33–56 (2013).

³ A. Doll, E. Bordignon, B. Joseph, R. Tschaggelar, and G. Jeschke, "Liquid state DNP for water accessibility measurements on spin-labeled membrane proteins at physiological temperatures," J. Magn. Reson. 222, 34–43 (2012).

- ⁴T. F. Segawa, M. Doppelbauer, L. Garbuio, A. Doll, Y. O. Polyhach, and G. Jeschke, "Water accessibility in a membrane-inserting peptide comparing Overhauser DNP and pulse EPR methods," J. Chem. Phys. 144(19), 194201 (2016).
- ⁵T. Überrück, O. Neudert, K.-D. Kreuer, B. Blümich, J. Granwehr, S. Stapf, and S. Han, "Effect of nitroxide spin probes on the transport properties of Nafion membranes," Phys. Chem. Chem. Phys. 20(41), 26660-26674 (2018).
- ⁶J. H. Ortony, C.-Y. Cheng, J. M. Franck, R. Kausik, A. Pavlova, J. Hunt, and S. Han, "Probing the hydration water diffusion of macromolecular surfaces and interfaces," New J. Phys. 13(1), 015006 (2011).
- ⁷B. D. Armstrong, M. D. Lingwood, E. R. McCarney, E. R. Brown, P. Blümler, and S. Han, "Portable X-band system for solution state dynamic nuclear polarization," Magn. Reson. 191(2), 273-281 (2008).
- ⁸ J. M. Franck, R. Kausik, and S. Han, "Overhauser dynamic nuclear polarizationenhanced NMR relaxometry," Microporous Mesoporous Mater. 178, 113-118
- O. Neudert, D. G. Zverev, C. Bauer, P. Blümler, H. W. Spiess, D. Hinderberger, and K. Münnemann, "Overhauser DNP and EPR in a mobile setup: Influence of magnetic field inhomogeneity," Appl. Magn. Reson. 43(1-2), 149-165 (2012).
- ¹⁰T. Überrück, M. Adams, J. Granwehr, and B. Blümich, "A compact X-Band ODNP spectrometer towards hyperpolarized ¹H spectroscopy," J. Magn. Reson. 314, 106724 (2020).
- 11 J. M. Franck and S. Han, "Overhauser dynamic nuclear polarization for the study of hydration dynamics, explained," in Biological NMR Part B, Methods in Enzymology, edited by A. J. Wand (Academic Press, 2019), Vol. 615, pp. 131–175. ¹²V. Denysenkov and T. Prisner, "Liquid state dynamic nuclear polarization probe with Fabry-Perot resonator at 9.2 T," J. Magn. Reson. 217, 1-5 (2012).
- ¹³P. Neugebauer, J. G. Krummenacker, V. P. Denysenkov, C. Helmling, C. Luchinat, G. Parigi, and T. F. Prisner, "High-field liquid state NMR hyperpolarization: A combined DNP/NMRD approach," Phys. Chem. Chem. Phys. 16(35), 18781-18787 (2014).
- ¹⁴D. Sezer, M. J. Prandolini, and T. F. Prisner, "Dynamic nuclear polarization coupling factors calculated from molecular dynamics simulations of a nitroxide radical in water," Phys. Chem. Chem. Phys. 11(31), 6626-6637 (2009).
- ¹⁵M. G. Concilio, M. Soundararajan, L. Frydman, and I. Kuprov, "High-field solution state DNP using cross-correlations," J. Magn. Reson. 326, 106940 (2021).
- 16 A. Krahn, P. Lottmann, T. Marquardsen, A. Tavernier, M.-T. Türke, M. Reese, A. Leonov, M. Bennati, P. Hoefer, F. Engelke, and C. Griesinger, "Shuttle DNP spectrometer with a two-center magnet," Phys. Chem. Chem. Phys. 12(22), 5830-5840 (2010).
- ¹⁷K. G. Valentine, G. Mathies, S. Bédard, N. V. Nucci, I. Dodevski, M. A. Stetz, T. V. Can, R. G. Griffin, and A. J. Wand, "Reverse micelles as a Platform for dynamic nuclear polarization in solution NMR of proteins," J. Am. Chem. Soc. 136(7), 2800-2807 (2014).
- ¹⁸A. Dey and A. Banerjee, "Unusual overhauser dynamic nuclear polarization behavior of fluorinated alcohols at room temperature," J. Phys. Chem. B 123, 10463 (2019).
- ¹⁹T. J. Keller, A. J. Laut, J. Sirigiri, and T. Maly, "High-resolution Overhauser dynamic nuclear polarization enhanced proton NMR spectroscopy at low magnetic fields," J. Magn. Reson. 313, 106719 (2020).
- $^{\mathbf{20}}\mathrm{E.}$ O. Stejskal and J. Schaefer, "Comparisons of quadrature and single-phase Fourier transform NMR," J. Magn. Reson. 14(2), 160-169 (1974).
- ²¹E. O. Stejskal and J. Schaefer, "Data routing in quadrature FT NMR," J. Magn. Reson. 13(2), 249-251 (1974).
- ²²D. I. Hoult and R. E. Richards, "Critical factors in the design of sensitive high resolution nuclear magnetic resonance spectrometers," Proc. R. Soc. A 344(1638), 311-340 (1975).
- ²³G. Bodenhausen, R. Freeman, and D. L. Turner, "Suppression of artifacts in two-dimensional J spectroscopy," J. Magn. Reson. 27(3), 511-514 (1977).
- ²⁴A. D. Bain, "Coherence levels and coherence pathways in NMR. A simple way to design phase cycling procedures," J. Magn. Reson. 56(3), 418-427 (1984).
- ²⁵G. Bodenhausen, H. Kogler, and R. R. Ernst, "Selection of coherence-transfer pathways in NMR pulse experiments," J. Magn. Reson. **58**(3), 370–388 (1984). ²⁶N. Ivchenko, C. E. Hughes, and M. H. Levitt, "Multiplex phase cycling,"
- J. Magn. Reson. 160(1), 52-58 (2003).

- ²⁷J. Schlagnitweit, M. Horničáková, G. Zuckerstätter, and N. Müller, "MQD—multiplex-Quadrature detection in multi-dimensional ChemPhysChem 13(1), 342-346 (2012).
- ²⁸J. H. Baltisberger, B. J. Walder, E. G. Keeler, D. C. Kaseman, K. J. Sanders, and P. J. Grandinetti, "Communication: Phase incremented echo train acquisition in NMR spectroscopy," J. Chem. Phys. 136(21), 211104 (2012).
- $^{\mathbf{29}}$ A. Wokaun and R. R. Ernst, "Selective detection of multiple quantum transitions in NMR by two-dimensional spectroscopy," Chem. Phys. Lett. 52(3), 407-412
- ³⁰Z. Gan and H.-T. Kwak, "Enhancing MQMAS sensitivity using signals from multiple coherence transfer pathways," J. Magn. Reson. 168(2), 346-351 (2004).
- ³¹C. A. Waudby, M. Ouvry, B. Davis, and J. Christodoulou, "Two-dimensional NMR lineshape analysis of single, multiple, zero and double quantum correlation experiments," J. Biomol. NMR 74(1), 95-109 (2020).
- 32 A. Schweiger and G. Jeschke, Principles of Pulse Electron Paramagnetic Resonance (Oxford University Press, 2001), ISBN: 978-0-19-850634-8.
- 33 J. Gorcester and J. H. Freed, "Two-dimensional Fourier-transform electronspin-resonance correlation spectroscopy," J. Chem. Phys. 88(8), 4678-4693
- ³⁴J. M. Franck, S. Chandrasekaran, B. Dzikovski, C. R. Dunnam, and J. H. Freed, "Focus: Two-dimensional electron-electron double resonance and molecular motions: The challenge of higher frequencies," J. Chem. Phys. 142(21), 212302
- 35 B. Blümich, "Low-field and benchtop NMR," J. Magn. Reson. 306, 27-35
- ³⁶M. Maiwald, H. H. Fischer, Y.-K. Kim, K. Albert, and H. Hasse, "Quantitative high-resolution on-line NMR spectroscopy in reaction and process monitoring," J. Magn. Reson. 166(2), 135–146 (2004).
- 37 Y.-Y. Lin, S. Ahn, N. Murali, W. Brey, C. R. Bowers, and W. S. Warren, "Highresolution, >1 GHz NMR in unstable magnetic fields," Phys. Rev. Lett. 85(17), 3732-3735 (2000).
- ³⁸M. G. Raymer, A. H. Marcus, J. R. Widom, and D. L. P. Vitullo, "Entangled photon-pair two-dimensional fluorescence spectroscopy (EPP-2DFS)," J. Phys. Chem. B 117(49), 15559-15575 (2013).
- ³⁹ S.-H. Shim, D. B. Strasfeld, E. C. Fulmer, and M. T. Zanni, "Femtosecond pulse shaping directly in the mid-IR using acousto-optic modulation," Opt. Lett. 31(6), 838 (2006).
- ⁴⁰J. C. Dean and G. D. Scholes, "Coherence spectroscopy in the condensed phase: Insights into molecular structure, environment, and interactions," Acc. Chem. Res. 50(11), 2746-2755 (2017).
- ⁴¹S. Mukamel, Principles of Nonlinear Optical Spectroscopy (Oxford University Press, New York, 1995).
- ⁴²R. R. Ernst, G. Bodenhausen, and A. Wokaun, *Principles of Nuclear Magnetic* Resonance in One and Two Dimensions (Clarendon Press, 1987), ISBN: 978-0-19-855629-9
- $^{\mathbf{43}}\mathrm{M}$. Rance and R. A. Byrd, "Obtaining high-fidelity spin-12 powder spectra in anisotropic media: Phase-cycled Hahn echo spectroscopy," J. Magn. Reson. 52(2), 221-240 (1983).
- ⁴⁴P. Callaghan, *Principles of Nuclear Magnetic Resonance Microscopy*, revised ed. (Clarendon Press, Oxford, 2011, ISBN: 978-0-19-853997-1, pp. 73-74.
- 45 J. Franck, A. Beaton, and A. Guinness, "Pyspecdata," http://github.com/ jmfrancklab/pyspecdata/, 2016.
- $^{\mathbf{46}}$ A. Bax, M. Ikura, L. E. Kay, and G. Zhu, "Removal of F_1 baseline distortion and optimization of folding in multidimensional NMR spectra," J. Magn. Reson. 91(1),
- ⁴⁷G. Zhu, D. A. Torchia, and A. Bax, "Discrete fourier transformation of NMR signals. The relationship between sampling delay time and spectral baseline," J. Magn. Reson. A 105(2), 219-222 (1993).
- ⁴⁸A. Bax and D. Marion, "Improved resolution and sensitivity in ¹H-detected heteronuclear multiple-bond correlation spectroscopy," J. Magn. Reson. 78(1), 186-191 (1988).
- ⁴⁹J. Cavanagh, W. J. Fairbrother, A. G. P. III, and N. J. Skelton, Protein NMR Spectroscopy: Principles and Practice (Academic Press, 1996), ISBN: 978-0-12-164490-1, pp. 177-178.

- ⁵⁰R. P. Futrelle and D. J. McGinty, "Calculation of spectra and correlation functions from molecular dynamics data using the fast Fourier transform," Chem. Phys. Lett. **12**(2), 285–287 (1971).
- ⁵¹ H. de Brouwer, "Evaluation of algorithms for automated phase correction of NMR spectra," J. Magn. Reson. **201**(2), 230–238 (2009).
- ⁵²F. C. Leone, L. S. Nelson, and R. B. Nottingham, "The folded normal distribution," Technometrics **3**(4), 543–550 (1961).
- ⁵³E. E. Najbauer and L. B. Andreas, "Correcting for magnetic field drift in magic-angle spinning NMR datasets," J. Magn. Reson. 305, 1–4 (2019).
- ⁵⁴S. B. Kim, Z. Wang, and B. Hiremath, "A Bayesian approach for the alignment of high-resolution NMR spectra," Ann. Oper. Res. **174**(1), 19–32 (2010).
- ⁵⁵ D. Ha, J. Paulsen, N. Sun, Y.-Q. Song, and D. Ham, "Scalable NMR spectroscopy with semiconductor chips," Proc. Natl. Acad. Sci. U. S. A. 111(33), 11955–11960 (2014).
- ⁵⁶ K. A. Veselkov, J. C. Lindon, T. M. D. Ebbels, D. Crockford, V. V. Volynkin, E. Holmes, D. B. Davies, and J. K. Nicholson, "Recursive segment-wise peak alignment of biological ¹H NMR spectra for improved metabolic biomarker recovery," Anal. Chem. 81(1), 56–66 (2009).
- ⁵⁷F. Savorani, G. Tomasi, and S. B. Engelsen, "icoshift: A versatile tool for the rapid alignment of 1D NMR spectra," J. Magn. Reson. 202(2), 190–202 (2010).
- ⁵⁸T. J. Keller and T. Maly, "Overhauser dynamic nuclear polarization (ODNP)-enhanced two-dimensional proton NMR spectroscopy at low magnetic fields," Magn. Res. **2**(1), 117–128 (2021).
- ⁵⁹ J. M. Franck, J. A. Scott, and S. Han, "Nonlinear scaling of surface water diffusion with bulk water viscosity of crowded solutions," J. Am. Chem. Soc. **135**(11), 4175–4178 (2013).
- ⁶⁰G. H. Weiss, R. K. Guptaj, J. A. Ferretti, and E. D. Becker, "The choice of optimal parameters for measurement of spin-lattice relaxation times. I. Mathematical formulation," J. Magn. Reson. **37**(3), 369–379 (1980).
- ⁶¹ S. Hoyer and J. Hamman, "xarray: N-D labeled arrays and datasets in Python," J. Open Res. Software 5(1), 10 (2017).
- 62 P. Virtanen, R. Gommers, T. E. Oliphant, M. Haberland, T. Reddy, D. Cournapeau, E. Burovski, P. Peterson, W. Weckesser, J. Bright, S. J. van der Walt, M. Brett, J. Wilson, K. J. Millman, N. Mayorov, A. R. J. Nelson, E. Jones, R. Kern, E. Larson, C. J. Carey, İ. Polat, Y. Feng, E. W. Moore, J. VanderPlas, D. Laxalde, J. Perktold, R. Cimrman, I. Henriksen, E. A. Quintero, C. R. Harris, A. M. Archibald, A. H. Ribeiro, F. Pedregosa, P. van Mulbregt, and SciPy 1.0 Contributors, "SciPy 1.0: Fundamental algorithms for scientific computing in Python," Nat. Methods 17, 261–272 (2020).
- ⁶³K. Poelke and K. Polthier, "Domain coloring of complex functions: An implementation-oriented introduction," IEEE Comput. Graph. Appl. **32**(5), 90–97 (2012).
- ⁶⁴D. Foster, C. Kind, P. J. Ackerman, J. S. B. Tai, M. R. Dennis, and I. I. Smalyukh, "Two-dimensional skyrmion bags in liquid crystals and ferromagnets," Nat. Phys. 15, 655 (2019).
- ⁶⁵ X. Yu, M. Mostovoy, Y. Tokunaga, W. Zhang, K. Kimoto, Y. Matsui, Y. Kaneko, N. Nagaosa, and Y. Tokura, "Magnetic stripes and skyrmions with helicity reversals," Proc. Natl. Acad. Sci. U. S. A. 109(23), 8856–8860 (2012).
- ⁶⁶C. A. Meriles, D. Sakellariou, and A. Pines, "Broadband phase modulation by adiabatic pulses," J. Magn. Reson. 164(1), 177–181 (2003).
- ⁶⁷J. M. Franck, V. Demas, R. W. Martin, L.-S. Bouchard, and A. Pines, "Shimmed matching pulses: Simultaneous control of rf and static gradients for inhomogeneity correction," J. Chem. Phys. 131(23), 234506 (2009).
- ⁶⁸ J. D. Hunter, "Matplotlib: A 2D graphics environment," Comput. Sci. Eng. **9**(3), 90–95 (2007).
- ⁶⁹G. Drobny, A. Pines, S. Sinton, D. P. Weitekamp, and D. Wemmer, "Fourier transform multiple quantum nuclear magnetic resonance," Faraday Symp. Chem. Soc. **13**, 49 (1978).
- ⁷⁰C. R. Harris, K. J. Millman, S. J. van der Walt, R. Gommers, P. Virtanen, D. Cournapeau, E. Wieser, J. Taylor, S. Berg, N. J. Smith, R. Kern, M. Picus, S. Hoyer, M. H. van Kerkwijk, M. Brett, A. Haldane, J. F. del Río, M. Wiebe, P. Peterson, P. Gérard-Marchant, K. Sheppard, T. Reddy, W. Weckesser, H. Abbasi, C. Gohlke, and T. E. Oliphant, "Array programming with NumPy," Nature 585(7825), 357–362 (2020).

- ⁷¹Y. Hibino, K. Sugahara, Y. Muro, H. Tanaka, T. Sato, and Y. Kondo, "Simple and low-cost tabletop NMR system for chemical-shift-resolution spectra measurements," J. Magn. Reson. **294**, 128–132 (2018).
- ⁷² K. Chonlathep, T. Sakamoto, K. Sugahara, and Y. Kondo, "A simple and low-cost permanent magnet system for NMR," J. Magn. Reson. 275, 114–119 (2017).
- 73 Note that the ordering of the dimensions in the \times expression and in the function are meaningful with respect to the code and implies the ordering of the data dimensions following a "C-type" (as opposed to "Fortran-type") convention, such that datapoints with adjacent indices along the right/innermost dimension reside in adjacent memory locations, while adjacent values in the left/outermost dimension reside further apart in memory.
- ⁷⁴J. Keeler, *Understanding NMR Spectroscopy* (John Wiley & Sons, 2011), ISBN: 978-1-119-96493-3.
- ⁷⁵M. H. Levitt, "The signs of frequencies and phases in NMR," J. Magn. Reson. **126**(2), 164–182 (1997).
- ⁷⁶M. H. Levitt and O. G. Johannessen, "Signs of frequencies and phases in NMR: The role of radiofrequency mixing," J. Magn. Reson. 142(1), 190–194 (2000).
- 77 The instrument constructed from these nonspecialized test and measurement equipment suffered from two drawbacks: first, a data size limitation and, second, slow communication between programmed commands and actual execution on the hardware. For a spectrometer constructed from nonspecialized components, higher-end test and measurement equipment with a larger storage memory could address the first limitation, as could a standard analog quadrature mixer and filter scheme, both of which are beyond the scope of this study. The second limitation may be overcome with test and measurement instruments providing USB 3.0 capabilities.
- ⁷⁸O. Neudert, H.-P. Raich, C. Mattea, S. Stapf, and K. Münnemann, "An Alderman–Grant resonator for S-band dynamic nuclear polarization," J. Magn. Reson. 242, 79–85 (2014).
- ⁷⁹S. Ahola, J. Perlo, F. Casanova, S. Stapf, and B. Blümich, "Multiecho sequence for velocity imaging in inhomogeneous rf fields," J. Magn. Reson. **182**(1), 143–151 (2006).
- ⁸⁰ Q. Bao, J. Feng, L. Chen, F. Chen, Z. Liu, B. Jiang, and C. Liu, "A robust automatic phase correction method for signal dense spectra," J. Magn. Reson. 234, 82–89 (2013).
- ⁸¹ M. Sawall, E. von Harbou, A. Moog, R. Behrens, H. Schröder, J. Simoneau, E. Steimers, and K. Neymeyr, "Multi-objective optimization for an automated and simultaneous phase and baseline correction of NMR spectral data," J. Magn. Reson. 289, 132–141 (2018).
- ⁸² D. D. Traficante and D. Ziessow, "A new apodization function for resolution enhancement with a minimum loss of sensitivity," J. Magn. Reson. 66(1), 182–186 (1986).
- ⁸³C. R. Pacheco and D. D. Traficante, "Two new window functions for long acquisition times," J. Magn. Reson. A **120**(1), 116–120 (1996).
- ⁸⁴V. A. Mandelshtam, "FDM: The filter diagonalization method for data processing in NMR experiments," Prog. Nucl. Magn. Reson. Spectrosc. 38(2), 159–196 (2001).
- 85 J. C. Hoch, "Beyond Fourier," J. Magn. Reson. 283, 117-123 (2017).
- ⁸⁶M. A. Zambrello, A. D. Schuyler, M. W. Maciejewski, F. Delaglio, I. Bezsonova, and J. C. Hoch, "Nonuniform sampling in multidimensional NMR for improving spectral sensitivity," Methods 138–139, 62–68 (2018).
- 87 S. G. Hyberts, K. Takeuchi, and G. Wagner, "Poisson-gap sampling and forward maximum entropy reconstruction for enhancing the resolution and sensitivity of protein NMR data," J. Am. Chem. Soc. 132(7), 2145–2147 (2010).
- ⁶⁸A. S. Stern, K. B. Li, and J. C. Hoch, "Modern spectrum analysis in multidimensional NMR spectroscopy: Comparison of linear-prediction extrapolation and maximum-entropy reconstruction," J. Am. Chem. Soc. **124**(9), 1982–1993 (2002).
- ⁸⁹ M. Levien, M. Reinhard, M. Hiller, I. Tkach, M. Bennati, and T. Orlando, "Spin density localization and accessibility of organic radicals affect liquid-state DNP efficiency," Phys. Chem. Chem. Phys. 23(8), 4480–4485 (2021).
- ⁹⁰ M. Levien, M. Hiller, I. Tkach, M. Bennati, and T. Orlando, "Nitroxide derivatives for dynamic nuclear polarization in liquids: The role of rotational diffusion," J. Phys. Chem. Lett. 11(5), 1629–1635 (2020).

- ⁹¹ A. Jerschow and N. Müller, "Efficient simulation of coherence transfer pathway selection by phase cycling and pulsed field gradients in NMR," J. Magn. Reson. 134(1), 17–29 (1998).
- ⁹² K. R. Metz, M. M. Lam, and A. G. Webb, "Reference deconvolution: A simple and effective method for resolution enhancement in nuclear magnetic resonance spectroscopy," Concepts Magn. Reson. 12(1), 21–42 (2000).
- spectroscopy," Concepts Magn. Reson. 12(1), 21–42 (2000).

 93 X. Tang, H. Ong, K. Shannon, and W. S. Warren, "Simultaneous acquisition of multiple orders of intermolecular multiple-quantum coherence images," Magn. Reson. Imaging 21(10), 1141–1149 (2003).
- ⁹⁴S. Saxena and J. H. Freed, "Absorption lineshapes in two-dimensional electron spin resonance and the effects of slow motions in complex fluids," J. Magn. Reson. 124(2), 439–454 (1997).
- ⁹⁵B. Dzikovski, V. V. Khramtsov, S. Chandrasekaran, C. Dunnam, M. Shah, and J. H. Freed, "Microsecond exchange processes studied by two-dimensional ESR at 95 GHz," J. Am. Chem. Soc. **142**(51), 21368–21381 (2020).
- ⁹⁶W. Hofbauer, K. A. Earle, C. R. Dunnam, J. K. Moscicki, and J. H. Freed, "High-power 95 GHz pulsed electron spin resonance spectrometer," Rev. Sci. Instrum. 75(5), 1194–1208 (2004).